

Influence of the Quasi-Biennial Oscillation and Sea Surface Temperature Variability on Downward Wave Coupling in the Northern Hemisphere

SANDRO W. LUBIS

GEOMAR Helmholtz Centre for Ocean Research Kiel, Kiel, Germany

KATJA MATTHES

GEOMAR Helmholtz Centre for Ocean Research Kiel, and Christian-Albrechts Universität zu Kiel, Kiel, Germany

NOUR-EDDINE OMRANI

*Geophysical Institute, University of Bergen, and Bjerknes Centre for Climate Research, Bergen, Norway,
and GEOMAR Helmholtz Centre for Ocean Research Kiel, Kiel, Germany*

NILI HARNIK

*Department of Geophysical, Atmospheric and Planetary Sciences, Tel Aviv University, Tel Aviv, Israel,
and Department of Meteorology, Stockholm University, Stockholm, Sweden*

SEBASTIAN WAHL

GEOMAR Helmholtz Centre for Ocean Research Kiel, Kiel, Germany

(Manuscript received 6 March 2015, in final form 24 January 2016)

ABSTRACT

Downward wave coupling occurs when an upward-propagating planetary wave from the troposphere decelerates the flow in the upper stratosphere and forms a downward reflecting surface that redirects waves back to the troposphere. To test this mechanism and potential factors influencing the downward wave coupling, three 145-yr sensitivity simulations with NCAR's Community Earth System Model [CESM1(WACCM)], a state-of-the-art high-top chemistry–climate model, are analyzed. The results show that the quasi-biennial oscillation (QBO) and SST variability significantly impact downward wave coupling. Without the QBO, the occurrence of downward wave coupling is significantly suppressed. In contrast, stronger and more persistent downward wave coupling occurs when SST variability is excluded.

The above influence on the occurrence of downward wave coupling is mostly due to a direct influence of the QBO and SST variability on stratospheric planetary wave source and propagation. The strengths of the tropospheric circulation and surface responses to a given downward wave coupling event, however, behave differently. The surface anomaly is significantly weaker (stronger) in the experiment with fixed SSTs (without QBO), even though the statistical signal of downward wave coupling is strongest (weakest) in this experiment. This apparent mismatch is explained by the differences in the strength of the synoptic-scale eddy–mean flow feedback and the possible contribution of SST anomalies in the North Atlantic during the downward wave coupling event. The weaker synoptic-scale eddy–mean flow feedback and the absence of the positive NAO-related SST-tripole pattern in the fixed SST experiment are consistent with a weaker tropospheric response to downward wave coupling. The results highlight the importance of synoptic-scale eddies in setting the tropospheric response to downward wave coupling.

 Supplemental information related to this paper is available at the Journals Online website: <http://dx.doi.org/10.1175/JAS-D-15-0072.s1>.

Corresponding author address: Sandro W. Lubis, GEOMAR Helmholtz Centre for Ocean Research Kiel, Düsternbrooker Weg. 20, 24105 Kiel, Germany.
E-mail: slubis@geomar.de

DOI: 10.1175/JAS-D-15-0072.1

1. Introduction

The vertical transport of energy via planetary-scale waves, forced by orography and land–ocean heating asymmetries, represents an important source of mutual dynamic coupling between the stratosphere and troposphere. The waves transport total eddy momentum and heat fluxes and therefore lead to a deviation of the stratospheric mean state from radiative equilibrium. An intensification of these planetary-scale waves occurs in winter, in the presence of westerly winds weaker than a critical value that depends on the horizontal scale of the waves (Charney and Drazin 1961; Eliassen and Palm 1961; Matsuno 1970). The variability of the stratospheric polar vortex during winter is primarily driven by the interaction between tropospheric forced planetary waves and the stratospheric mean flow. The strength of the polar vortex is further determined by a combination of natural and anthropogenic forcings, such as the quasi-biennial oscillation (QBO) of equatorial stratospheric winds, variations in sea surface temperatures (SSTs), volcanic eruptions, the 11-yr solar cycle, and anthropogenic emissions (e.g., Holton and Tan 1980; van Loon and Labitzke 1987; Robock 2000; Gray et al. 2010; Schimanke et al. 2013).

The dependence of the strength of stratospheric polar vortex on the phase of the tropical QBO was first proposed by Holton and Tan (1980). In the so-called Holton–Tan (HT) mechanism, the vortex remains in an undisturbed, colder state when the QBO is in its westerly phase and favors a disturbed, warmer state during the east phase of the QBO. This is related to the shifting of the critical line toward the Northern Hemisphere (NH) subtropics, followed by a poleward displacement of the planetary waveguide during the QBO east phase, which directs more waves to polar regions and decelerates the vortex through enhanced wave–mean flow interactions. The warmer and more disturbed polar vortex during the QBO east phase is often reflected with a higher frequency of sudden stratospheric warming (SSW) events (Labitzke 1982). Lu et al. (2014) recently illustrated this process by showing that a formation of a midlatitude waveguide during the QBO east phase provides a favorable pathway for more upward- (35°–50°N, 30–200 hPa) and northward- (35°–60°N, 20–5 hPa) propagating planetary waves, which eventually dissipate and break in the high-latitude upper to middle stratosphere. However, Garfinkel et al. (2012) argue that the QBO-induced secondary meridional circulation is more important than the subtropical critical line for the polar QBO signals during the east phase of the QBO. The secondary QBO circulation acts as a barrier for planetary wave propagation in the middle to upper stratosphere during the

easterly phase, resulting in enhanced wave convergence in the polar stratosphere and therefore a more disturbed polar vortex. Even though the evidence is inconclusive as to which mechanism dominates the QBO–vortex interaction, both above-mentioned mechanisms contribute to the probability of the breakdown of the vortex.

The SST variations can impact the stratospheric polar vortex through different mechanisms. For example, van Loon and Labitzke (1987) first presented how tropical SSTs can influence the stratospheric polar vortex during the warm phase of ENSO (i.e., El Niño). They showed that warm ENSO events are associated with increased frequency of SSWs and therefore a warmer and more disturbed polar vortex. This was further confirmed by some general circulation model (GCM) studies (e.g., Hamilton 1993; Manzini et al. 2006) showing that the warmings observed during El Niño years are associated with the amplification of upward planetary wave convergence. More recently, using the global coupled climate model GFDL CM3, Li and Lau (2013) showed that enhancement or attenuation of the amplitudes of zonal wavenumbers 1 and 2 during ENSO events modulates the frequency of occurrence of stratospheric polar vortex anomalies. By combining ENSO–QBO effects on the vortex state, Calvo et al. (2009) showed that weak and warm polar vortices occur during warm ENSO in the late winter during both QBO phases. In addition to ENSO, other mechanisms including large-scale North Atlantic temperature (Omriani et al. 2014; Keenlyside and Omriani 2014; Omriani et al. 2016), extratropical SST in the Pacific basin (Hurwitz et al. 2012), and sea ice (Jaiser et al. 2013) are also important for stratospheric variability through ocean–atmosphere coupling mechanisms.

Over the past two decades, the role of downward-propagating planetary waves, in particular the wave reflection, has been continuously investigated to elucidate mechanisms for stratosphere–troposphere coupling (e.g., Harnik and Lindzen 2001; Perlwitz and Harnik 2003; Harnik 2009; Shaw and Perlwitz 2013). The so-called downward wave coupling (DWC) describes the stratospheric downward wave reflection that impacts the troposphere. DWC occurs when upward-propagating planetary waves from the troposphere decelerate the flow in the upper stratosphere and form a negative meridional potential vorticity (PV) gradient and a vertical reflecting surface as well as a vertically bounded high-latitude meridional waveguide. During NH winter, reflecting surfaces typically develop above 10 hPa on a weekly time scale. They act as a stratospheric barrier for upward-propagating waves. In the high-latitude stratosphere, a meridional waveguide forms at around 50°–80°N and further directs downward-propagating stratospheric waves toward the troposphere (Harnik

and Lindzen 2001; Shaw et al. 2010). Recently, Shaw and Perlwitz (2013) defined a wave coupling index based on stratospheric eddy meridional wave-1 heat flux to examine the impact of DWC on the NH winter troposphere (see also Dunn-Sigouin and Shaw 2015). They show that multiple stratospheric wave reflection events are associated with a strong polar vortex and a positive phase of a North Atlantic–like oscillation in the troposphere. However, the factors which influence DWC and its subsequent impacts on the tropospheric circulation are still unclear. We try to address this question within this study.

The goal of the present study is to examine to what extent natural forcing factors, such as the QBO and SST variability, influence the occurrence and variability of DWC. For that purpose, we perform a set of sensitivity experiments with the fully coupled Community Earth System Model, version 1.0.2, with the Whole Atmosphere Community Climate Model [CESM1(WACCM)], where we systematically switch on and off the influence of the QBO or the interactively calculated SSTs and sea ice. We also examine how these natural forcing factors affect the impact of DWC on the tropospheric circulation. The paper is organized as follows. A description of the model, experiments, reanalysis data, and our statistical–dynamical approach are provided in section 2. In section 3, we discuss the general assessment of DWC variability in CESM1(WACCM) and compare it to reanalysis data, while section 4 deals with the response of the mean climate behavior and DWC characteristics with respect to the QBO and variable SSTs and sea ice. In section 5, the implication of DWC for the troposphere–surface system is examined based on extreme negative stratospheric wave-1 heat flux (DWC) events. We also discuss the differences of tropospheric changes associated with DWC in the absence of the QBO and SST variability. We close in section 6 with a summary of our results.

2. Data, model experiments, and analysis

a. Model, experiments, and reanalysis data

NCAR’s Community Earth System Model, version 1.0.2, is a fully coupled climate model consisting of atmosphere [optionally NCAR’s Community Atmosphere Model (CAM) or WACCM], ocean (POP), land (CLM), and sea ice (CICE) components, based on the Community Climate System Model (CCSM4; Gent et al. 2011). The atmospheric component of CESM used in this study is the Whole Atmosphere Community Climate Model, version 4 (Marsh et al. 2013), a high-top chemistry–climate model, which is an extension of NCAR’s Community Atmosphere Model. WACCM has a horizontal resolution of 1.9° latitude \times 2.5°

longitude and 66 vertical levels from the surface to the lower thermosphere (~ 140 km and $\sim 5.1 \times 10^{-6}$ hPa). Interactive chemistry is calculated with the 3D chemical transport Model of Ozone and Related Chemical Tracers, version 3 (MOZART-3; Kinnison et al. 2007). It includes the O_x , NO_x , HO_x , ClO_x , and BrO_x chemical families, along with CH_4 species within the chemical and physical processes in the troposphere through the lower thermosphere (i.e., fully interactive and fully coupled chemistry and physics). Additional processes important for the mesosphere and lower thermosphere, such as ion chemistry, auroral processes, extreme ultraviolet, and non-local thermodynamic equilibrium radiation are also implemented (Marsh et al. 2007).

To investigate the influence of the QBO and the SST variability on DWC, three CESM1(WACCM) simulations were performed by systematically switching on and off particular forcing factors (Table 1). The control simulation (CTL) covers the period 1955–2099 (i.e., a 145-yr control run). This experiment is run with an interactive ocean and a QBO nudging in the tropical stratosphere between 22° S and 22° N following Matthes et al. (2010). The effects of QBO nudging in CESM1 (WACCM) on extratropical and high-latitude dynamics resemble observations. In particular, the planetary wave propagation and residual circulation responses to the forcing from the equatorial QBO agree well with ERA-40 (Hansen et al. 2013). The QBO is projected into the future by developing Fourier coefficients for the QBO time series based on climatological values of Giorgetta¹ from the past records (1954–2004). To exclude external anthropogenic influences, all anthropogenic forcings, such as greenhouse gases (GHGs), ozone depleting substances (ODS), or airplane emissions were kept constant at the 1960s level (i.e., annual cycle values were repeated for the whole modeling time).

The second simulation is the fixed (noninteractive) SST–sea ice experiment (FSST), which spans the period from 1955 to 2099 (145-yr simulated period). The FSST is the same as the CTL, except the underlying SSTs and sea ice are held constant for each year based on climatological monthly varying SSTs and sea ice of the CTL experiment. This simulation therefore neglects any effects of interannual and intraseasonal varying SSTs–sea ice and excludes any atmosphere–ocean–sea ice feedbacks. While SST variability influences the stratospheric planetary wave source, and thus the strength of DWC, the coupling to the ocean and sea ice can influence the response of the troposphere to a given DWC event. The

¹ http://www.pa.op.dlr.de/CCMVal/Forcings/qbo_data_ccmval_u_profile_195301-200412.html.

TABLE 1. Summary of CESM experiments and ERA data.

Experiment	Period	QBO	GHGs + ODSs	SSTs–sea ice
CTL	1955–2009 (145 yr)	Nudged	Fixed at 1960s level	Interactively
FSST	1955–2009 (145 yr)	Nudged	Fixed at 1960s level	Fixed ^a
NOQBO	1955–2009 (145 yr)	No	Fixed at 1960s level	Interactively
All forcing	1958–2005 (48 yr)	Nudged	Obs	Interactively
ERA	1958–2005 (48 yr) ^b	Obs	Obs	Obs

^a SSTs follow the climatological cycle of the CTL.

^b Includes 1958–1978 from the ERA-40 and 1979 onward from the ERA-Interim.

third simulation uses the same settings as CTL but without the QBO nudging for the 145-yr simulated period (1955–2009) (NOQBO). The NOQBO experiment exhibits constant easterly winds in the equatorial stratosphere with an amplitude of about -10 m s^{-1} . Finally, the comparison of the CTL with the NOQBO and the FSST experiments allows us to investigate the relative role of the QBO and the SST variability on DWC and its subsequent impacts on the troposphere.

To evaluate how realistic the DWC is in CESM1 (WACCM), daily 3D geopotential, wind, and temperature fields from the combined European Centre for Medium-Range Weather Forecast (ECMWF) ERA-40 (Uppala et al. 2005) and the ERA-Interim (Dee et al. 2011) (hereinafter referred to as ERA) from January 1958 to December 2005 (48 yr) and altitudes from the surface to 1 hPa (23 vertical pressure levels) were used (see Table 1). The CESM simulation for this comparison employs the most realistic setting [i.e., natural and anthropogenic forcings (for details see Table 1)]. The time-varying anthropogenic forcings (GHG and ODS) were obtained from the observational records until 2005. This simulation is referred to as “all forcings” in the following. Currently, only one ensemble per CESM experiment was performed, as performing separate simulations for each type of forcing with interactive ocean and interactive atmospheric chemistry up to the lower thermosphere is computationally very expensive.

b. Statistical–dynamic diagnosis

In this study, the impact of the QBO and SST variability on DWC are examined by using both statistical and dynamical approaches, which include the wave geometry diagnostic, the time-lagged singular value decomposition (SVD), and the transformed Eulerian mean (TEM) diagnostics.

1) WAVE GEOMETRY

To diagnose the wave propagation characteristics of a two-dimensional zonal-mean basic state, the wave geometry diagnostic of Harnik and Lindzen (2001) was employed in this study. Principally, this diagnostic

partitions the widely used refractive index (n_r^2 ; e.g., Charney and Drazin 1961; Matsuno 1970) into vertical (m) and meridional (l) wavenumber components by solving the conservation of the quasigeostrophic potential vorticity (QGPV) equation in spherical coordinates. This separation provides the barriers of wave propagation in the vertical and meridional directions. For a nonisothermal atmosphere, a general n_r^2 decomposition for waves with a zonal wavenumber k and a phase speed c is written as follows (for details, see Harnik and Lindzen 2001):

$$n_r^2 \equiv \frac{N^2}{f^2} \left\{ \frac{\bar{q}_y}{\bar{u} - c} - k^2 + f^2 \frac{e^{z/2H}}{N} \frac{\partial}{\partial z} \left[\frac{e^{-z/2H}}{N} \frac{\partial}{\partial z} (e^{z/2H} N) \right] \right\} \\ \equiv m^2 + \frac{N^2}{f^2} l^2, \quad (1)$$

where \bar{q}_y is the meridional gradient of zonal-mean PV, calculated following Matsuno (1970) as

$$\bar{q}_y \equiv \beta - \frac{1}{a^2} \frac{\partial}{\partial \phi} \left[\frac{1}{\cos \phi} \frac{\partial (\bar{u} \cos \phi)}{\partial \phi} \right] - \frac{f^2}{\rho_0} \frac{\partial}{\partial z} \left(\frac{\rho_0}{N^2} \frac{\partial \bar{u}}{\partial z} \right). \quad (2)$$

Expansion of the last term on the left-hand side of Eq. (2) gives:

$$-\frac{f^2}{\rho_0} \frac{\partial}{\partial z} \left(\frac{\rho_0}{N^2} \frac{\partial \bar{u}}{\partial z} \right) \equiv \left(\frac{f^2}{HN^2} + \frac{f^2}{N^4} \frac{\partial N^2}{\partial z} \right) \frac{\partial \bar{u}}{\partial z} - \frac{f^2}{N^2} \frac{\partial^2 \bar{u}}{\partial z^2}, \quad (3)$$

where N^2 is the buoyancy frequency, and β is the variation of the Coriolis parameter with latitude. The results of an n_r^2 decomposition are interpreted similarly as discussed by Charney and Drazin (1961) and Matsuno (1970). The waves propagate in the vertical (meridional) direction where $m^2 > 0$ ($l^2 > 0$), are evanescent where $m^2 < 0$ ($l^2 < 0$), and are reflected where $m^2 = 0$ ($l^2 = 0$). It is worth noting that if the waves propagate with the background flow ($\bar{u} = c$), then there exist critical

surfaces ($l^2, m^2 \rightarrow \infty$) that tend to absorb or over-reflect the propagating waves² (e.g., McIntyre and Palmer 1983). To retain pure real–imaginary wavenumber quantities, all averages in time and space were calculated by squaring the wavenumber and then taking a square root of the respective values [e.g., $\langle l \rangle = \text{sign}(\langle l^2 \rangle) \times (|\langle l^2 \rangle|)^{1/2}$].

2) TIME-LAGGED SINGULAR VALUE DECOMPOSITION

To study the linear statistical relationship between tropospheric and stratospheric geopotential height associated with a single zonal wavenumber, a time-lagged SVD of the coupled fields was used as in Perlwitz and Harnik (2003). This technique identifies pairs of leading EOFs and PCs, which account for a fraction of the covariance between two single zonal waves jointly (for details see Perlwitz and Harnik 2003). The daily temporal expansion coefficients were calculated as the weighted linear projection of data at each grid point onto their corresponding EOFs, as follows (Bretherton et al. 1992):

$$A^k(t) = \sum_{i=1}^{M_p} V_i^k P_i(t) = \mathbf{V}_k^T P(t) \quad \text{and} \quad (4)$$

$$B^k(t + \tau) = \sum_{j=1}^{M_s} U_j^k S_j(t + \tau) = \mathbf{U}_k^T S(t + \tau). \quad (5)$$

Here, P and S denote tropospheric and stratospheric zonal wavenumber-1 geopotential heights (Z-ZWN1), M is number of grid points, and \mathbf{V}_k and \mathbf{U}_k are the left and right singular vectors at mode k , respectively. The time-lagged SVD analysis is repeated for entire seasons with 3-month overlapping periods only for zonal wave 1, as it represents the dominant source of DWC (Perlwitz and Harnik 2003; Shaw et al. 2010). The tropospheric field is held fixed at 500 hPa, and the respective stratospheric levels are shifted in such a way that a negative (positive) time lag indicates that the stratospheric (tropospheric) wave fields are leading.

3) PLANETARY WAVE FORCING OF THE MEAN FLOW

To quantify the drag exerted by planetary-scale waves on the mean flow, the Eliassen–Palm flux (Andrews et al. 1987) and the Plumb 3D wave activity flux (Plumb 1985) in spherical log-pressure coordinates are used also in this study. The detailed formulation is described in the appendix.

3. Evaluation of DWC in CESM1(WACCM)

a. DWC behavior during midwinter

We begin our evaluation with an analysis of DWC in the all-forcings experiment of CESM1(WACCM) from 1958 to 2005 and a comparison to reanalysis data. We first focus on the northern midwinter January–March (JFM) mean, as it represents the most dynamically active season. The background wind is westerly; planetary wave activity is large; thus, its vertical propagation is enhanced (e.g., Charney and Drazin 1961; Lorenz and Hartmann 2003); and therefore dynamical coupling between the stratosphere and the troposphere is largest (e.g., Baldwin and Dunkerton 2001; Perlwitz and Harnik 2003, Shaw et al. 2010).

Figure 1 compares the JFM climatological zonal-mean zonal wind and zonal-mean temperature between the CESM1(WACCM) simulation and ERA. The stratospheric polar night jet in the model is significantly stronger and broader throughout the stratosphere. The midlatitude jet at 1 hPa is about 5 m s^{-1} stronger in the model, and the 20 m s^{-1} isoline reaches further down to 20 km (Fig. 1c). The subtropical tropospheric jet is also about 5 m s^{-1} stronger in the model as compared to reanalysis. Consistent with the positive wind bias in the stratosphere is the cold bias in the polar stratosphere (Figs. 1b,d), which is a common bias in chemistry–climate models (SPARC CCMVal 2010). In addition to the zonal wind, Figs. 1a and 1c also shows the wave geometry; that is, the configurations of meridional waveguide and vertical reflecting surfaces. The shaded areas (unshaded) indicate regions where waves cannot (can) propagate in meridional [l^2 (blue)] and vertical [m^2 (red)] directions. In general, the wave geometry structure in CESM1(WACCM) is in fairly good agreement with ERA, except that the meridional waveguide in the model is slightly narrower between 45° and 60°N in the troposphere, which may be related to biases in the meridional structure of modeled zonal-mean winds in this region. In the upper stratosphere (above 5 hPa), a vertical reflecting surface appears at around 65° – 80°N in the model, which suggest that the configuration of the modeled stratospheric polar night jet during JFM allows downward reflection of planetary waves.

To characterize up- and downward propagation of wave-1 anomalies, correlations from the time-lagged leading SVD mode between wave-1 height fluctuations at a tropospheric pressure level (500 hPa) and four different stratospheric pressure levels (50, 20, 30, and 10 hPa) in both CESM1(WACCM) and ERA data are shown in Fig. 2. This investigation is an example for wave 1, which contributes most to the DWC. Positive lags denote upward wave coupling from the troposphere

² In the nonlinear limit, waves undergo cycles of absorption, reflection, or over-reflection near the critical surface when $K^2 \equiv k^2 + l^2 + (f_0^2/N^2)m^2$ increases toward infinity.

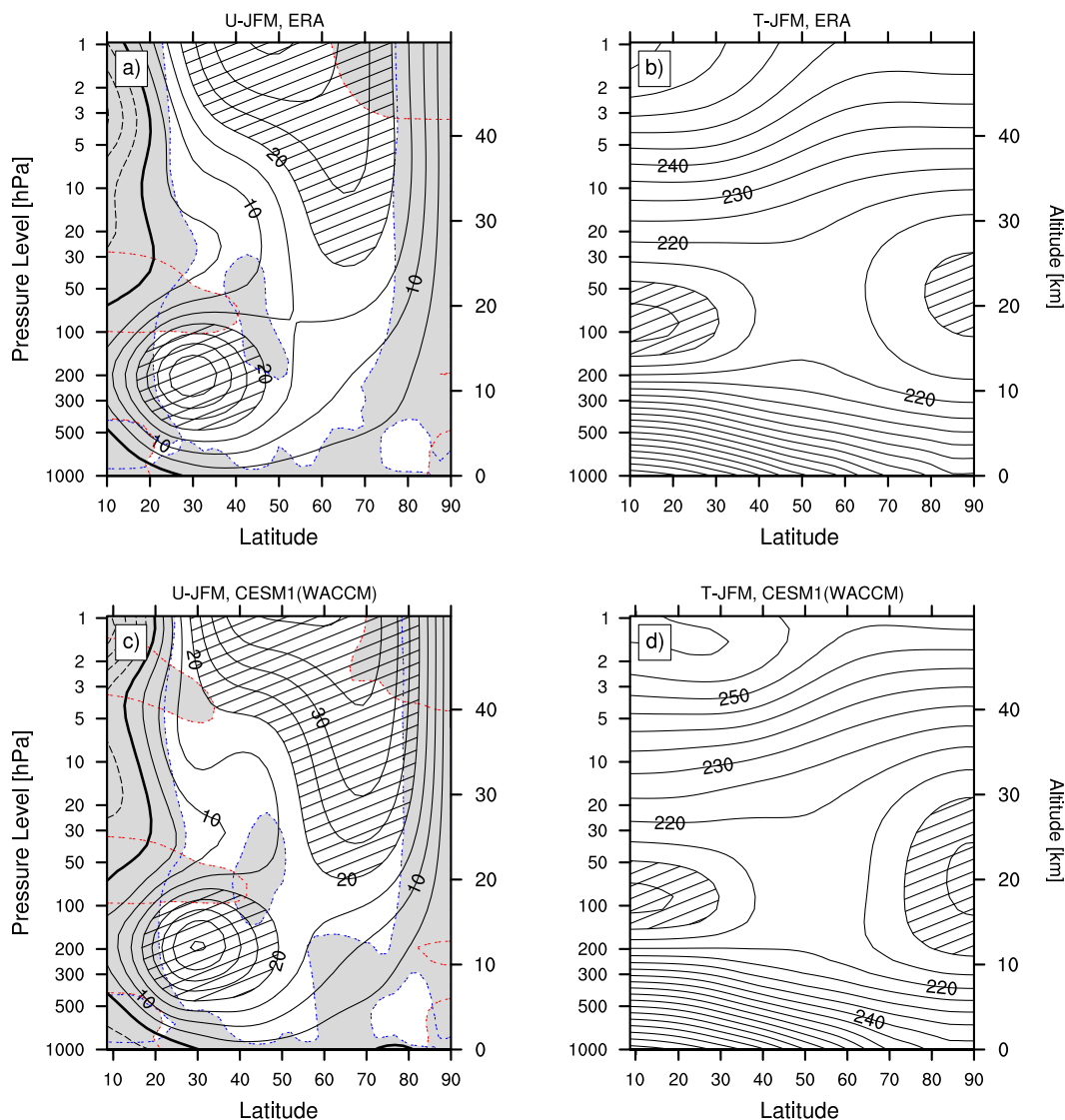


FIG. 1. JFM average of the zonal-mean zonal wind and zonal-mean temperature between 10° and 90°N and 1000 and 1 hPa for the (a),(b) ERA and (c),(d) CESM1(WACCM) from 1958 to 2005. Shading in (a) and (c) indicates regions of wave evanescence in the meridional ($l < 0$) and vertical ($m < 0$) directions. Contour intervals are 5 m s^{-1} and 5 K for wind and temperature, respectively. The regions where the wind (temperature) exceeds 20 m s^{-1} (210 K) are hatched. The red (blue) dashed contours indicate the vertical reflecting surface (meridional waveguide) when $m = 0$ ($l = 0$). The zero contour lines are plotted in thick solid black.

to the stratosphere, whereas negative lags denote downward wave coupling from the stratosphere to the troposphere. The time-lagged SVD correlations in CESM1(WACCM) exhibit a fairly similar twofold-peaked structure as those observed in ERA (Figs. 2a,d). In particular, the maximum positive correlations (i.e., the troposphere leads the stratosphere) occur one day early and are higher than the observed peaks in ERA. This suggests that the simulated upward wave coupling between the troposphere and the stratosphere has a faster vertical group velocity than in ERA. Consistent with the

upward wave-energy flux propagation, there is a westward phase tilt with height (Figs. 2c,f; Table 2). Note that the group velocity of a quasi-stationary Rossby wave is tangent to phase lines in a horizontal plane, where phase lines associated with the upward- (downward-) propagating Rossby wave group velocity are tilted westward (eastward) with height (Charney and Drazin 1961). In addition, the associated wave-1 amplitudes at 10 and 500 hPa in the model are larger compared to ERA and therefore are consistent with higher SVD correlation peaks at positive time lags.

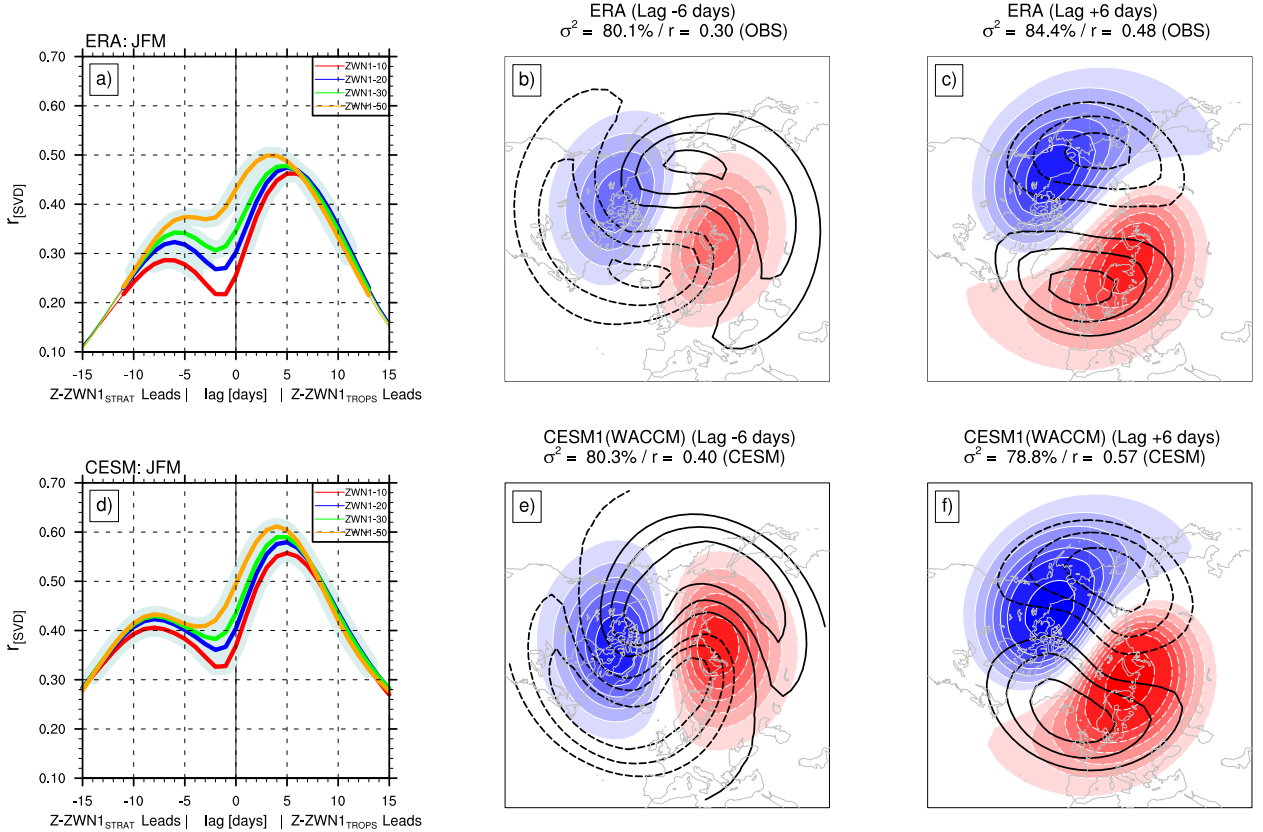


FIG. 2. (left) Lagged correlations of temporal expansion coefficients (a_k, b_k) between the leading wave-1 SVD mode (Z-ZWN1) at 500 hPa (fixed level) and four stratospheric levels [50 (yellow), 30 (green), 20 (blue), and 10 hPa (red)] for (a) ERA and (d) CESM1 (WACCM) during mid-late winter (JFM). The 99% and 95% significance levels are denoted with light gray shading and thicker lines, respectively. (center) Heterogeneous regression patterns at 10 hPa (color shaded) and 500 hPa (contours) associated with downward wave coupling (Z-ZWN1₁₀ leads Z-ZWN1₅₀₀ by 6 days) for (b) ERA and (e) CESM1(WACCM). The contour interval is 30 m (color shading) for Z-ZWN1 at 10 hPa, and 5 m for Z-ZWN1 at 500 hPa. (right) As in (b), (e), but for upward wave coupling (Z-ZWN1₅₀₀ leads Z-ZWN1₁₀ by 6 days). The 0-m contour is omitted.

In the period when the stratosphere is leading (negative lags), the correlation peak in CESM1(WACCM) is again higher and the time lag is slightly longer compared to ERA (Fig. 2d). Although there is virtually no separation in correlation peaks at negative time lags for stratospheric levels below 10 hPa in the model, the eastward phase tilt with height consistent with downward flux of wave energy associated with DWC can still be seen in CESM1(WACCM) (Table 2; Fig. 2e). A similar characteristic of DWC signals has also been found in Shaw et al. (2010, their Fig. 7) using the high-top CMAM version. Shaw et al. (2010) argue that no separation in peaks of DWC signals may be caused by the internal dynamical damping processes in the model. In CESM1(WACCM), the amplitudes of the wave-1 pattern associated with DWC in the stratosphere and troposphere are larger compared to ERA, which is again consistent with higher correlations found in the model when the stratosphere is leading (Fig. 2d). In addition, we also applied the

statistical and wave geometry diagnostics for wave-2 coupling in ERA and CESM (not shown). While the formation of reflecting surfaces for wave-2 is found during midwinter, we do not find evidence for a second peak in SVD correlations associated with DWC. Perlwitz and Harnik (2003) previously found a similar behavior and argued that this is because of a short propagating period of wave 2 into the midstratosphere (of about 2 days), which makes it hard to separate statistically the downward from the upward wave-2 propagating signals.

In summary, CESM1(WACCM) is able to capture DWC during NH midwinter (JFM). However, there are still small discrepancies in the time lags, phase shifts, and strength of DWC. This could be due to the common model biases in the background circulation which feeds back on the wave dynamics and wave-mean flow interaction (e.g., Charney and Drazin 1961; Lorenz and Hartmann 2003). In particular, the stronger background wind in CESM1(WACCM) (Fig. 1) can be associated

TABLE 2. The phase differences $d\lambda$ at 65°N between the associated SVD wave-1 patterns at 500 hPa (fixed) and various stratospheric levels (50, 30, and 10 hPa) in the ERA and all-forcing experiment from CESM1(WACCM) from 1958 to 2005. Negative (positive) time lag indicates that the stratospheric (tropospheric) wave fields are leading.

Height range (hPa)	Lag (days)	$d\lambda$ (°E)	
		ERA	All forcings
500–10	–6	108.4	114.2
500–30	–5	81.6	90.3
500–50	–4	60.3	53.2
500–10	6	–133.5	–122.7
500–30	5	–102.3	–94.9
500–50	4	–78.1	–75.1

with stronger downward wave activity between the stratosphere and troposphere, as highlighted by [Perlwitz and Harnik \(2003\)](#) and [Shaw et al. \(2010\)](#).

b. Seasonal evolution of DWC

To completely assess the representation of DWC in CESM1(WACCM), we also examine its seasonal evolution by calculating SVD correlations (r_{SVD}) of Z-ZWN1 for corresponding PCs at each time lag for 3-month overlapping periods (Fig. 3). DWC events occur if the r_{SVD} at a negative time lag is highly statistically significant at the 99% level. Compared to ERA, DWC in CESM1(WACCM) persists throughout the winter (November–March, Fig. 3b) whereas it only occurs between January and March in ERA (Fig. 3a). In addition, the time scales of downward wave propagation in the model are relatively longer, which indicate a slower downward group velocity of Z-ZWN1 from the stratosphere to the troposphere.

To further understand the seasonal evolution of DWC in CESM1(WACCM) in comparison with ERA, we also consider the seasonal evolution of the wave geometry. Figure 4 highlights the climatological seasonal evolution of the meridional wavenumber (l^2) averaged between 16 and 24 km and the vertical wavenumber (m^2) averaged from 60° to 80°N for ERA (Figs. 4a,b) and CESM1(WACCM) (Figs. 4c,d). In ERA data, a meridional waveguide occurs only from January through March, with a meridional extent from 45° to 75°N (Fig. 4a), whereas in CESM1(WACCM) the meridional waveguide occurs earlier from November through March (Fig. 4c) and is slightly narrower with a meridional extent from 51° to 75°N. This narrower meridional waveguide potentially increases the occurrence of DWC in CESM1(WACCM), as it limits the meridional wave propagation into a subtropical critical surface. In addition, a narrower waveguide also implies the l^2 is larger, and the larger l^2 for a given index of refraction implies a smaller m^2 , thus leading to more downward reflection.

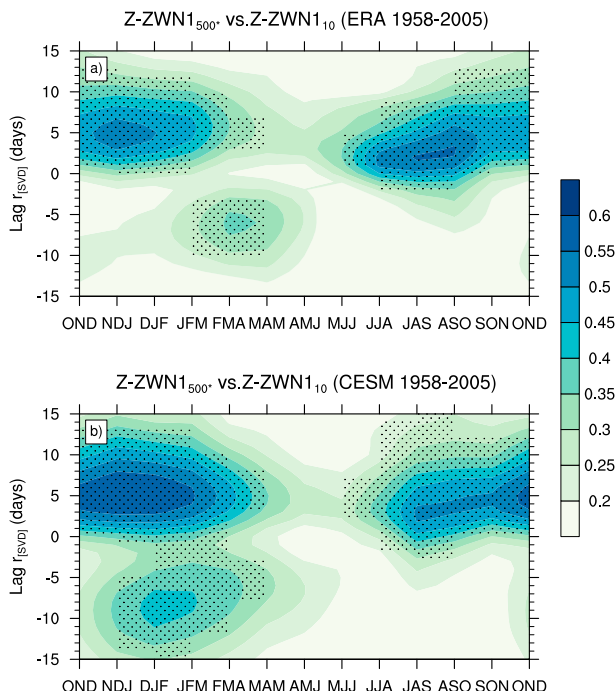


FIG. 3. Three-month overlapping periods of lagged SVD correlations between Z-ZWN1 at 500 and 10 hPa for (a) ERA and (b) CESM1(WACCM) from 1958 to 2005. Black dots represent statistically significant values at the 99% level. A negative (positive) time lag indicates that the stratospheric (tropospheric) wave field is leading.

Stratospheric vertical reflecting surfaces in ERA form in early winter (November–December) and during mid-winter (February–March) (Fig. 4b). The vertical reflecting surface is very high in the stratosphere (between 1–3 hPa) in November–December and very low from March onward. This wave geometry evolution is in qualitative agreement with previous finding by [Shaw et al. \(2010\)](#) using a 27-yr ERA dataset (note that about 21 more years of the combined ERA dataset have been included in our study). In contrast to ERA, the stratospheric reflecting surface in CESM1(WACCM) persists from early to late winter (October–November to March–April). The extended meridional waveguide and the longer persistence of vertical reflecting surfaces in CESM1(WACCM) as compared to ERA are consistent with the extended significant downward wave correlations in Fig. 3b from November through March. However, in October the stratospheric reflecting surface does not coincide with the meridional waveguide. The waves therefore disperse in the meridional direction and get absorbed in the subtropical critical surface, thus causing an absence of DWC signals during OND (Fig. 3b).

To summarize, our results show that the seasonal evolution of DWC in CESM1(WACCM) persists longer compared to ERA. This extension coincides with a

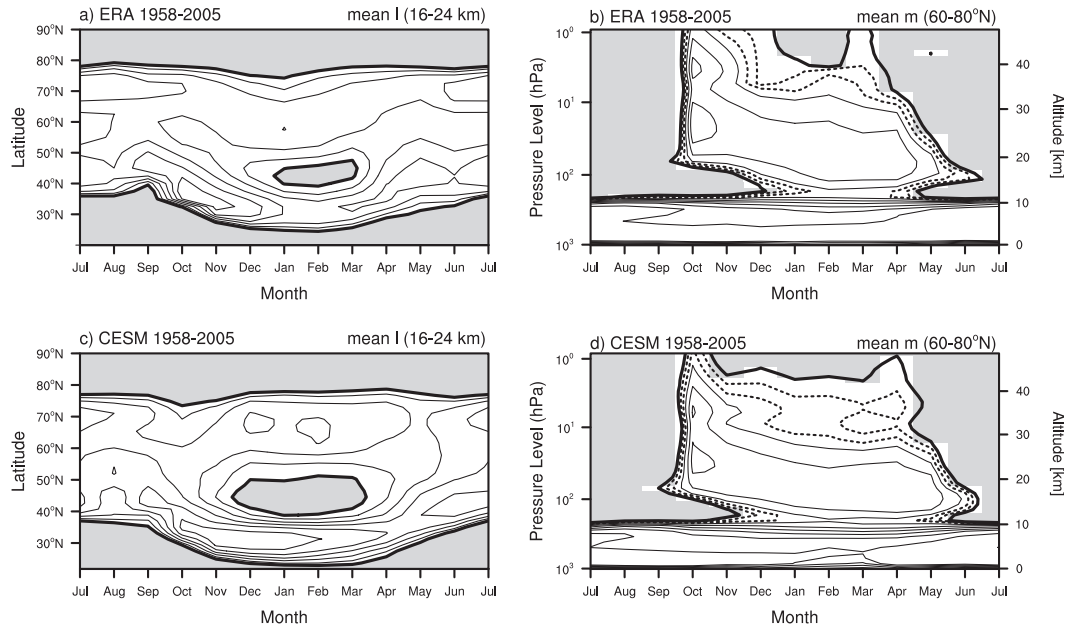


FIG. 4. The climatological seasonal cycle of the meridional and vertical wavenumbers averaged (a),(c) between 16 and 24 km and (b),(d) between 60° and 80°N for ERA and CESM1(WACCM), respectively. The meridional wavenumbers are contoured with 1 (solid) and 0.01 rad^{-1} (thick solid line). For the vertical wavenumber, the contours are shown at 0.01×10^{-5} (thick line), 0.02×10^{-5} and 0.04×10^{-5} (dashed lines), and $0.06\text{--}0.3 \times 10^{-5} \text{ m}^{-1}$ in jumps of $3 \times 10^{-5} \text{ m}^{-1}$ (thin lines). Finally, the gray shading indicates the regions of wave evanescence in meridional ($l < 0$) and vertical directions ($m < 0$).

persistent formation of a mid- to high-latitude meridional waveguide and a vertical reflecting surface at the same time, which allow more DWC to occur. The early onset of the wave geometry is consistent with a stronger background zonal-mean zonal wind in the model. These results emphasize that an accurate representation of the stratospheric mean states and wave geometries (l^2 and m^2) are necessary to properly represent the evolution of DWC in a climate model. This evaluation also suggests that the wave geometries and the DWC can be employed to examine the discrepancies of winter states between models and observations.

4. The influence of QBO and SST variability on DWC

In this section, the impact of removing QBO or specifying climatological seasonally varying SSTs on DWC is presented by first discussing their influences on the background winds, the wave coupling correlation and the seasonal variation of wave geometries.

a. Polar night jet strength

The two-way vertical (upward and downward) planetary wave propagation, which modifies the strength of the polar vortex, can be changed by the vertical and meridional structure of the zonally averaged zonal wind (Charney and

Drazin 1961; Limpasuvan and Hartmann 2000; Perlwitz and Harnik 2003). Therefore, it is important to first examine how the strength and structure of the background winds have changed in each of the experiments.

Figure 5 shows the zonal-mean zonal wind differences between the NOQBO and the CTL experiments for 3-month overlapping periods from November through April. Without the QBO nudging, the tropical stratospheric winds resemble a weak but persistent east QBO state throughout the year, with easterly winds of about -10 m s^{-1} . At high latitudes, the effect of removing the QBO and thus weak easterlies in the tropical lower stratosphere notably weakens the polar vortex. In particular, the zonal-mean zonal wind speed is significantly weaker by up to -2 m s^{-1} from November through February and shifts downward to 100 hPa in JFM. The QBO effect on the polar vortex weakens and loses significance from February to April (FMA) onward. The weakening of the stratospheric polar vortex in NOQBO experiment resembles the impact of the easterly phase of the QBO on the polar stratospheric vortex (e.g., Richter et al. 2011; Lu et al. 2014; Garfinkel et al. 2012). This is associated with a significantly increased upward wave propagation (which results in strong wave convergence) and redistribution the region of wave absorption (see Fig. S1).

In the fixed SSTs experiments, in contrast, the vortex is stronger and less disturbed (Figs. 5e–h). The zonal-mean

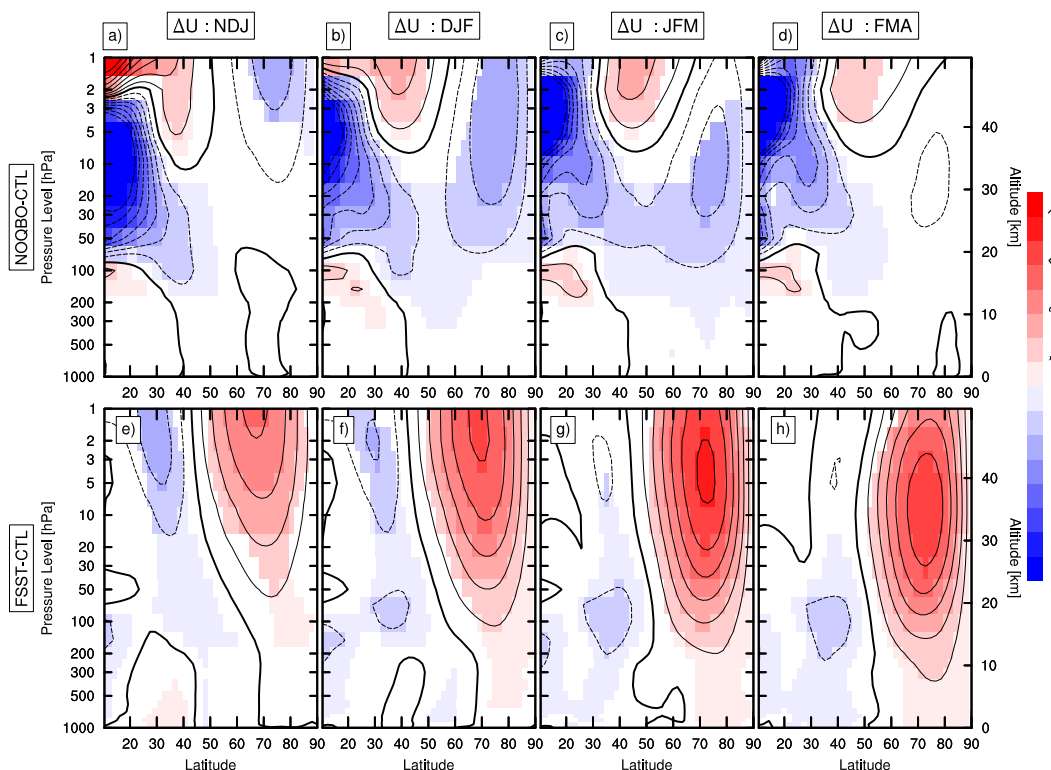


FIG. 5. The climatological zonal-mean wind differences between 10° and 90° N and 1000 and 1 hPa for (a)–(d) NOQBO – CTL and (e)–(h) FSST – CTL during (left to right) NDJ, DJF, JFM, and FMA. The contour interval is 1 m s^{-1} , and shaded areas represent regions with Student's t test values at the 95% significance level. The 0 m s^{-1} contour is plotted in thick solid black lines.

zonal wind exhibits a statistically significant increase of about $1\text{--}4 \text{ m s}^{-1}$ in the mid- to upper stratosphere in November–January (NDJ) and stays stronger up to 5 m s^{-1} in December–February (DJF). The positive zonal wind anomalies are strongest in JFM, with differences up to 6 m s^{-1} , and get weaker during FMA with a downward shift of the peak toward the surface. The strengthening of the stratospheric vortex in the FSST experiment is accompanied by a significant anomalous downward wave propagation and decreased wave dissipation/breaking in the stratosphere (Fig. S1).

In summary, the NOQBO and FSST experiments represent opposite responses on the polar vortex. The lack of the QBO (SST variability) in CESM1(WACCM) significantly weakens (strengthens) the stratospheric polar night jet. These changes in the mean state will interact with upward and downward planetary wave propagation. A strong (weak) background zonal-mean zonal wind in the model can be associated with a more (less) downward wave reflection in the stratosphere toward the troposphere.

b. Wave coupling correlations

To measure seasonal variations of DWC, 3-month overlapping correlation coefficients of the time-lagged

SVD between Z-ZWN1 at 500 hPa and at 10 hPa are computed throughout the seasons for the three different CESM1(WACCM) experiments (Figs. 6a–c), similar to Fig. 3. The DWC events occur if the correlation peaks at a negative time lag (when the stratospheric field is leading) and is statistically significant at the 99% level. The seasonal evolution of DWC in the CTL experiment is in reasonable agreement with the all-forcing CESM1(WACCM) experiment (including both natural and anthropogenic forcings), where DWC activity maximizes at about 6–7 days from DJF to FMA (cf. Fig. 3). Therefore, the focus in the subsequent analysis will be on the comparison between the CTL, NOQBO, and FSST experiments.

In the NOQBO experiment (Fig. 6b), DWC occurs over a shorter time period from January to March with a weaker correlation compared to that in the CTL experiment (Fig. 6a). On the other hand, DWC is significantly stronger and more persistent over a longer period of time (from November through April) in the FSST (Fig. 6c) as compared to the CTL and NOQBO experiments. In particular, the maximum correlation of DWC in the FSST experiment in JFM–FMA, when the polar night jet is strengthened and extends into the

troposphere (Figs. 5g–h). The statistically significant correlations in April–June to May–July (AMJ–MJJ) (Fig. 6c) are not related to downward wave reflection in the upper stratosphere, as the wave evanescence (region with negative refractive index) covers almost the whole NH stratosphere because of a reversal of the background winds during this period (not shown). The DWC can thus not explain the high correlation when the stratosphere leads in AMJ–MJJ, which might require other dynamical processes [e.g., nonlinear wave dynamics during final vortex breakdown (Shaw et al. 2010)]. Furthermore, to better understand the DWC changes between the CTL and NOQBO experiments, we also analyze the CTL experiment separately for east and west QBO seasons. Indeed, we find that the DWC signal is weaker in the CTL during east QBO and is much strengthened during west QBO (Fig. S3). This is consistent with weaker DWC signals in the NOQBO, since the tropical winds in this experiment resemble a weak persistent east-QBO state.

Based on the stratosphere–troposphere wave coupling correlations, we showed that in the absence of the QBO, the occurrence of DWC between stratosphere and troposphere is suppressed, and only weak DWC appears in JFM. Without SST variability, in contrast, the DWC is stronger and seasonally persistent from November to April. These results are consistent with differences in the climatological strength of the stratospheric polar night jet together with differences in planetary wave propagation and wave–mean flow interaction, which are all influenced by the QBO and SST variability (Figs. 5, S1, and S2).

c. Evolution of the wave geometry

To better understand the influence of the QBO and atmosphere–ocean coupling on the nature of DWC throughout the seasonal cycle, we consider the evolution of the wave geometry. Similar to Fig. 4, Fig. 7 shows the seasonal evolution of the zonal wave-1 meridional wavenumbers (l) averaged between 25 and 30 km (left) and the vertical wavenumbers (m) averaged between 60° and 80°N (right) for the three CESM1(WACCM) experiments. The vertical averaging of l from 25 to 30 km quantifies the equatorward boundary of the mid-stratospheric meridional waveguide, which limits equatorward propagation of extratropical waves. On the other hand, the meridional averaging of m between 60° and 80°N quantifies the vertical extent of the reflecting surfaces in the stratosphere.

The climatological seasonal evolution of the meridional wavenumber shows that, in the absence of QBO, the meridional waveguide exhibits a shorter seasonal persistence than in CTL (January–February to February–March in NOQBO vs November–December

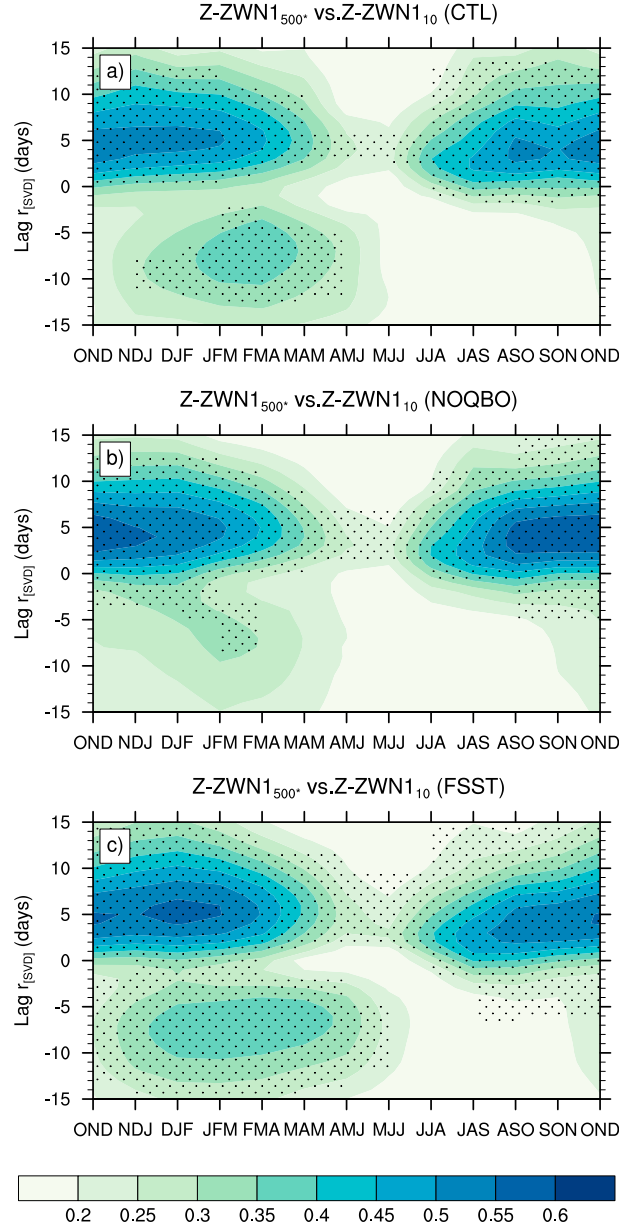


FIG. 6. Three-month overlapping periods of lagged SVD correlations between Z-ZWN1 at 500 and 10 hPa for (a) CTL, (b) NOQBO, and (c) FSST. Black dots represent values significant at the 99% level. A negative (positive) time lag indicates that the stratospheric (tropospheric) wave field is leading.

to February–March in CTL; Figs. 7a,b). Without SST variability, in contrast, the meridional waveguide undergoes a longer seasonal persistence as compared to the CTL (November–December to March–April in FSST vs November–December to February–March in CTL; Figs. 7a,c). This suggests that the wave reflection in the absence of SST variability may persist longer as a result of less meridional wave dispersion in the stratosphere.

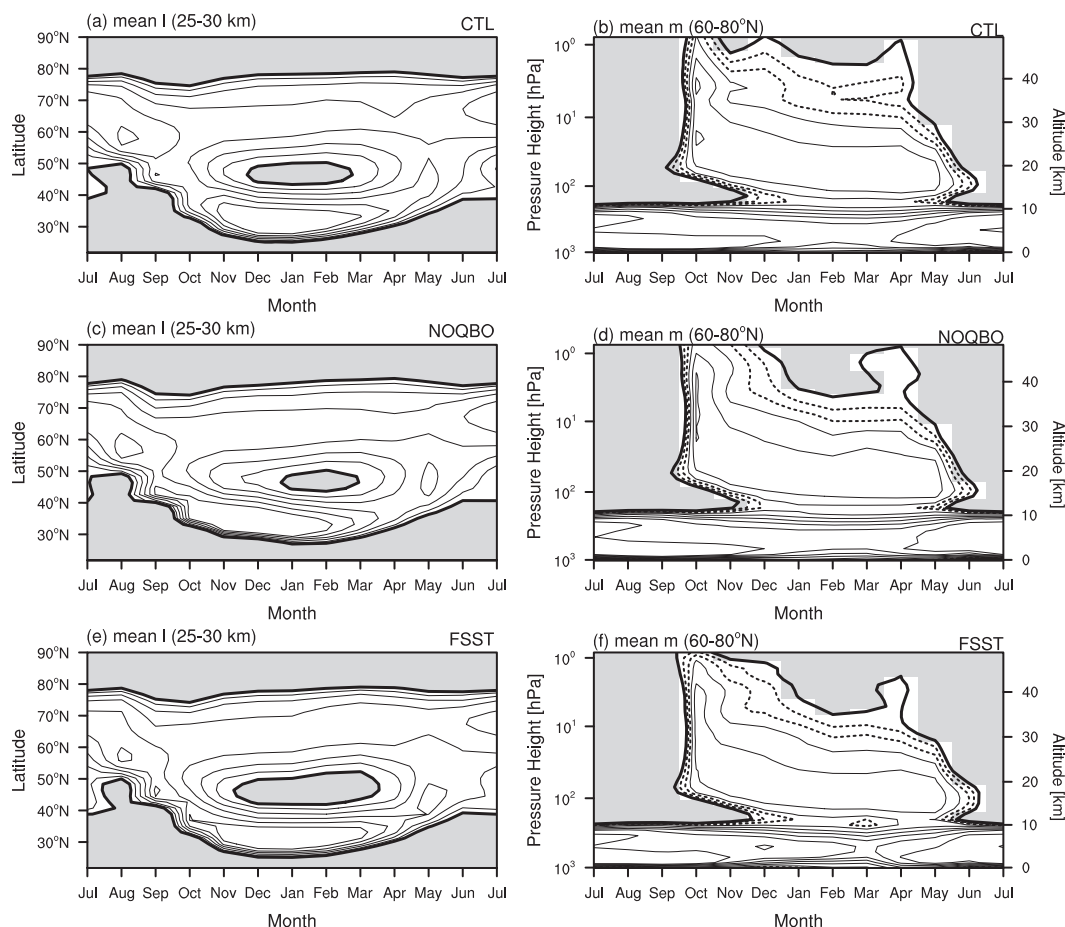


FIG. 7. As in Fig. 4, but the meridional wavenumbers are averaged between 25 and 30 km.

On the other hand, the climatological seasonal cycle of vertical wavenumbers shows that, without the QBO, vertical reflecting surfaces occur only from January to March (Fig. 7d). From May onward, the reflecting surface builds at very low altitudes because of a gradual descent of the zero wind line toward high latitudes after the polar vortex breakup. In contrast, without SST variability, the reflecting surface persists longer over an extended wintertime from October to April, as compared to CTL and NOQBO (Fig. 7f). The reflecting surfaces in November and December in the FSST are located at higher altitudes near 1 hPa compared to that in January–April. We note here that the higher reflecting surface in October occurs as a result of the strong background wind in the model, which exceeds the critical value and leads to negative refractive index (wave evanescence).

By combining the seasonal cycles of meridional and vertical wavenumbers in Fig. 7, the high-latitude meridional waveguide l in the absence of QBO is completely bounded above by a vertical reflecting surface m

from January to March [which is shorter, compared to CTL from November to March (Figs. 7a,b and 7c,d)]. This configuration coincides with the maximum DWC in Fig. 6b during JFM. In contrast, the wave geometry during November–December and April in NOQBO is not bounded (Figs. 7c,d). In particular, there is no meridional waveguide during these periods, and therefore, instead of propagating vertically, the waves can propagate meridionally into the subtropics where they encounter subtropical critical surfaces. These dynamical features are in fairly good agreement with the anomalous upward and equatorward direction of Eliassen–Palm (EP) flux vectors in the absence of the QBO (Figs. S1a–d).

On the other hand, without SST variability, the high-latitude meridional waveguide l is completely bounded above by a vertical reflecting surface m over an extended wintertime from November to April (Figs. 7e,f). This configuration supports a longer seasonal activity of DWC and is thus consistent with the persistent DWC signals in

Fig. 6c. An increased DWC activity is also in good agreement with an amplification of anomalous downward wave flux, which strengthens the downward wave propagation (Figs. S1e–h). As we noted previously, the high correlation in AMJ–MJJ for negative time lags (when the stratosphere is leading) is not related to DWC, as the wave geometry configuration during this period is not bounded by the meridional waveguide (**Fig. 7e**).

5. Impact of DWC on the troposphere–surface system

Our previous results showed that the absence of the QBO or SST variability significantly influence the strength of DWC during NH winter. Therefore, it is worthwhile to examine whether the absence of the QBO and SST variability affect the impact of DWC on the tropospheric circulation. We focus on the most active winter season JFM, as it is a favorable period for planetary wave coupling and a period where the CESM1 (WACCM) experiments exhibit significant DWC signals in the troposphere (see **Figs. 6a–c**).

a. Statistics of stratospheric wave-1 heat flux extremes

Previous studies have shown that a dynamical metric based on negative stratospheric wave-1 heat flux extremes, can be used to isolate the tropospheric impacts of DWC (**Shaw et al. 2014; Dunn-Sigouin and Shaw 2015**). The extreme negative (positive) high-latitude stratospheric heat flux events are defined as the days with a total (climatology plus anomaly) wave-1 meridional heat flux value (i.e., $\overline{v'T'}_{k=1}$)³ at 50 hPa averaged between 60° and 90°N below (above) the 10th (90th) percentile of the JFM distribution. In this section, we first examine the statistical distribution of total stratospheric wave-1 heat flux extremes and then quantify the relative occurrence of downward versus upward wave events among the model experiments.

The statistics of high-latitude wave-1 heat flux distribution for three CESM1(WACCM) experiments are listed in **Table 3**. The 10th (90th) percentile values in **Table 3** indicate the heat flux value below which 10% (90%) of each model's total heat flux distribution can be found. Consistent with our previous findings, the highest downward (upward) wave activity is seen in the FSST (NOQBO) experiment. In particular, without SST

TABLE 3. Kolmogorov–Smirnov (KS) two-sample test of $\overline{v'T'}_{k=1}$ (m s^{−1} K) averaged from 60° to 90°N at 50 hPa during JFM. The 10th (90th) percentile is the heat flux value below which 10% (90%) of the total distribution can be found. The *p* values shown are relative to the CTL.

Experiment	Mean	Std dev	10th percentile	90th percentile	<i>p</i> value
CTL	15.40	25.26	−10.22	49.15	1.00
FSST	12.71	22.60	−12.71	43.02	<0.05
NOQBO	16.70	27.11	−9.50	52.69	<0.07

variability, the wave-1 heat flux value at the 10th percentile is lower by about 24.4% (33.8%) compared to the CTL (NOQBO) experiment (**Table 3**), while without the QBO, the wave-1 heat flux at the 90th percentile is higher by 7.2% (22.5%) compared to the CTL (FSST, **Table 3**). Correspondingly, the mean value of the wave-1 heat flux of the NOQBO (FSST) experiment is higher (lower) than in the CTL experiment, which indicates an increased (decreased) climatological-mean upward wave activity in the stratosphere during wintertime. According to the random sampling of a Kolmogorov–Smirnov test, the distribution of the wave-1 heat flux in FSST (NOQBO) is significantly different from the CTL distribution at the 95% (93%) level (see *p* values in **Table 3**).

Figure 8 shows percentage (frequency) of extreme negative wave-1 heat flux events (*y* axis) versus extreme positive wave-1 heat flux events (*x* axis) between the NOQBO (triangles) and the FSST (asterisks) with respect to the CTL experiment at different stratospheric levels, that is, 70, 50, 30, and 10 hPa. Extreme negative (positive) heat flux days are defined as the days below (above) the 10th (90th) percentile values of the CTL experiment. It is clearly seen that the NOQBO (FSST) experiment shows clustering of higher frequency of days with extreme positive (negative) wave-1 heat fluxes at different stratospheric levels compared to the CTL. Extreme positive (negative) wave-1 heat flux events indicate strong net upward (downward) wave-1 activity in the NOQBO (FSST) experiment. This frequency of wave-1 heat flux events is in good agreement with statistically increased (decreased) occurrence of DWC in the FSST (NOQBO) experiment. The changes in frequency of extreme heat flux events are also consistent with the climatological differences in planetary wave propagation and wave–mean flow interaction among model experiments (**Fig. S1**). Further examination of the coupled structures (the SVD patterns at the times of maximum upward and downward coupling) shows that the amplitude of the waves varies between the different runs (largest for FSST and weakest for NOQBO); the phase differences between the stratospheric and tropospheric waves are similar for both time lags (**Table 4**; see

³ For pure plane waves, $\overline{v'T'}_{k=1}$ is proportional to the vertical group velocity of planetary waves by assuming wave activity density (Λ) is positive definite [e.g., in **Charney and Drazin (1961)**, $F_z \equiv c_{gz}\Lambda$, where $\Lambda \cong (\rho_o/4)[(\partial Q/\partial y)/(\bar{u} - c)^2]|\Psi_o|^2$]; that is, if $(\overline{v'T'}_{k=1} \propto c_{gz})$ and $\Lambda > 0$, thus $F_z < 0$ (downward-propagating wave).

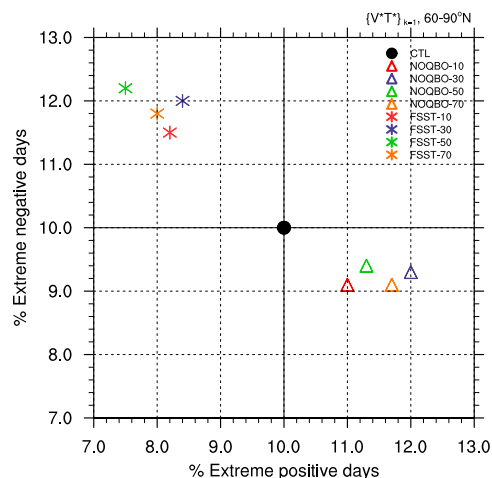


FIG. 8. Percentage (frequency) of extreme negative high-latitude averaged wave-1 heat flux events at 10-, 30-, 50-, and 70-hPa levels vs extreme positive events at the same levels during JFM for CTL, NOQBO, and FSST. See text for definition of negative and positive extremes.

also Figs. S4 and S5). Thus, the changes in the DWC correlations (e.g., Fig. 6) come both from a change in the frequency of occurrence of wave events and a change in the amplitude of the waves, but not from a difference in the phase tilt of the waves.

b. Impact on the tropospheric circulation

We now examine the impact of individual DWC events on the tropospheric circulation by looking at composites of various fields. An individual DWC event is identified as the day of minimum extreme negative heat flux value, where each central event must be separated by at least 15 days according to the time scale of planetary wave coupling⁴ (Perlitz and Harnik 2003). The composite anomalies are calculated as the deviations from the climatological seasonal cycle. The statistical significance of the composites is estimated using a Monte Carlo approach (Schreck et al. 2013) by randomly choosing 1000 combinations of N days, N being the number of composite members. Note that we focus on the tropospheric impacts in the North Atlantic region since there is a clear connection between that region and negative extreme stratospheric wave-1 heat flux values (Shaw and Perlitz 2013; Shaw et al. 2014; Dunn-Sigouin and Shaw 2015).

⁴ By using this definition, the composites of the total geopotential wave-1 structure for ERA and the three CESM1(WACCM) experiments exhibit a clear eastward phase tilt with height, which thus is consistent with downward propagation of wave activity from the stratosphere to the troposphere (Fig. S5).

TABLE 4. The phase differences $d\lambda$ at 65°N between the associated SVD wave-1 patterns at 500 hPa (fixed) and various stratospheric levels (50, 30, and 10 hPa) in CTL, NOQBO, and FSST from 1955 to 2009. Negative (positive) time lag indicates that the stratospheric (tropospheric) wave fields are leading.

Height range (hPa)	Lag (days)	$d\lambda$ (°E)		
		CTL	NOQBO	FSST
500–10	−6	106.4	104.8	109.3
500–30	−5	89.2	90.9	88.7
500–50	−4	66.0	68.7	66.7
500–10	6	−125.4	−129.6	−126.4
500–30	5	−101.7	−99.7	−100.4
500–50	4	−82.5	−81.4	−80.9

Figure 9 shows the composites of 500-hPa geopotential height (Figs. 9a–d), 700-hPa zonal-mean wind (Figs. 9e–h), and mean sea level pressure (Figs. 9i–l) anomalies north of 20°N during the time when DWC impact on the troposphere maximizes (i.e., 5-days average around the central date), for the ERA, CTL, NOQBO, and FSST experiments. On average, the impact of downward stratospheric wave activity in both ERA and CESM1(WACCM) experiments resembles the patterns projecting onto the positive phase of the North Atlantic Oscillation (NAO) (Hurrell et al. 2013). This is similar to the result shown by Shaw and Perlitz (2013), which has been related to DWC impact. In particular, the geopotential height anomalies exhibit a seesaw shape between mid- and high latitudes (Figs. 9a–d), while the tropospheric zonal wind anomalies reflect the strengthening and poleward shift of the tropospheric jet over the North Atlantic basin (Figs. 9e–h). The sea level pressure anomalies show a similar pattern as the 500-hPa geopotential height anomalies, indicating a quasi-barotropic tropospheric NAO-like structure in association with downward wave activity (Figs. 9i–l). The discrepancies between ERA and CESM1(WACCM) are mainly discernible over the North Atlantic basin, especially in its western half, where all associated surface responses in CESM1(WACCM) are relatively modest. Nevertheless, the main features associated with the positive NAO-like responses are relatively well captured in CESM1(WACCM) experiments.

Comparing all CESM1(WACCM) sensitivity experiments, it can be seen that without QBO nudging (Figs. 9c,g,k), the DWC's impact on the tropospheric circulation enhances significantly compared to that in the CTL experiment (Figs. 9b,f,j). In particular, the geopotential height anomalies exhibit a stronger amplitude over the Atlantic basin and correspondingly a strengthening and poleward shift of the tropospheric jet (Figs. 9b,c and Figs. 9f,g). The mean sea level pressure anomalies are stronger in the Atlantic basin

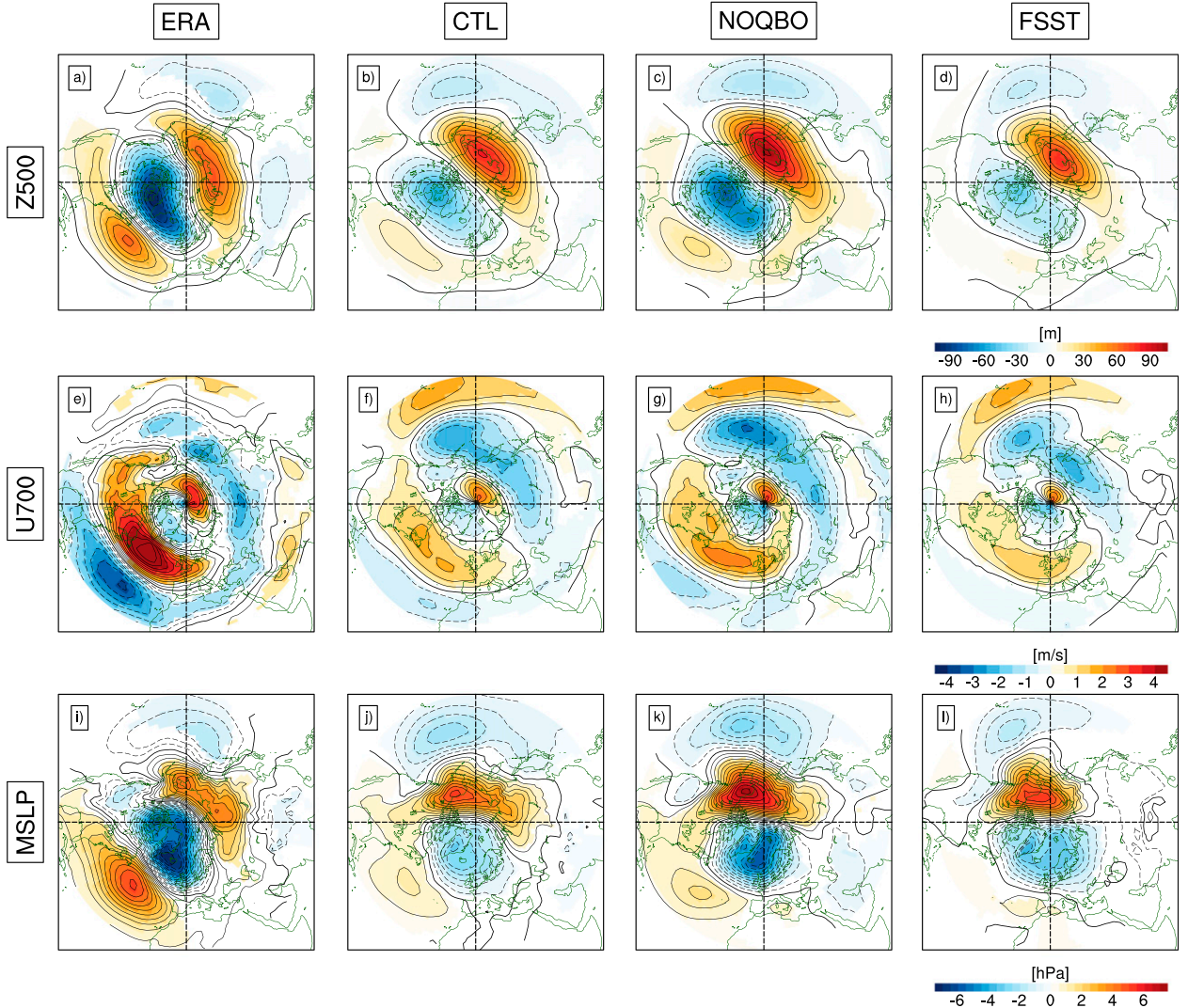


FIG. 9. The composites of (a)–(d) 500-hPa geopotential height, (e)–(h) 700-hPa zonal wind, and (i)–(l) mean sea level pressure anomalies during the period of maximum DWC impact on the troposphere (5-day average around the central date) in JFM for (left to right) ERA, CTL, NOQBO, and FSST. Contours (black) indicate the variances of (a)–(d) 500-hPa geopotential height (interval 500 m), (e)–(h) 700-hPa zonal wind (interval 2 m s^{-1}), and (i)–(l) mean sea level pressures (interval 0.5 hPa). The color shadings are only drawn for anomalies that are statistically significant at the 95% confidence level using a Monte Carlo approach.

compared to the CTL experiment, which is consistent with the strengthening of geopotential height anomalies aloft (Figs. 9k,c). In contrast, without SST variability, the surface influence of DWC in the North Atlantic basin is significantly weaker and prevails only over limited regions compared to those found in the CTL experiment (Figs. 9j,l). The poleward jet shift in the Atlantic basin (Fig. 9h) is weaker than in the CTL and NOQBO experiments (Figs. 9f,g), which is consistent with a weakening of geopotential height and mean sea level pressure anomalies over this region (Figs. 9d,l). These results have been verified to be robust to details of the composite calculation,

event definition,⁵ and the number of DWC events. In particular, by randomly choosing the same number of composite members N as in the CTL experiment, we find that weaker (stronger) surface signals associated with DWC in the FSST (NOQBO) experiments are robust and independent from the number of DWC events used in our composite (not shown).

⁵ The results are not sensitive to the choice of stratospheric pressure level of $\overline{v'T'}_{k=1}$ (e.g., 30 or 70 hPa), to the thresholds of extreme negative stratospheric $\overline{v'T'}_{k=1}$ (e.g., at 1st, 3rd, 5th, and 7th percentiles), and to the choice of significance levels (e.g., 99%).

A priori, one might expect the tropospheric and surface response to DWC to be stronger in the model runs for which the statistical signal of DWC is stronger and more persistent and for which the amplitude of the downward-propagating waves is stronger. However, we see that the opposite is true: a stronger tropospheric response is observed in the NOQBO experiment, for which the DWC signal is weakest, and vice versa for the FSST experiment. Indeed, the differences in acceleration of the flow because of planetary-scale waves during DWC events (Figs. 10a–d) are not able to explain the differences in the tropospheric responses between FSST and NOQBO experiments. The planetary-scale wave drag anomalies (color shading) in the North Atlantic basin are strongest in the FSST experiment and weakest in the NOQBO experiment. These differences would suggest a stronger response for FSST, but we get the opposite for tropospheric responses. Furthermore, these planetary-scale wave drag anomalies are located more poleward from the position of the westerly wind anomalies (Figs. 9e–h) and coincide partially with upward-propagating planetary-scale wave sources (see solid contour lines in the North Atlantic basin). This suggests that other factors besides the frequency and strength of the downward wave propagation from the stratosphere influence the strength of the tropospheric response. Other studies have shown that internal tropospheric dynamics involving feedbacks from synoptic-scale eddy activity are important for stratosphere–troposphere coupling (e.g., Song and Robinson 2004; Garfinkel et al. 2013; Kunz and Greatbatch 2013). We thus proceed to examine those feedbacks here.

Figure 11 shows the composites of the anomalous synoptic-scale horizontal component of the \mathbf{E} vectors,⁶ alongside its divergence at 250 hPa (representing the influence of the synoptic-scale eddies on the horizontal large scale flow; Figs. 11a–d), anomalous vertical component of the \mathbf{E} vectors at 700 hPa (representing the source of synoptic-scale eddies; Figs. 11e–h), anomalous Eady growth rate at 700-hPa (representing the baroclinicity of the mean flow; Figs. 11i–l), and anomalous synoptic geopotential height variance at 250 hPa (representing the storm-track strength; Figs. 11m–p). We see that the synoptic eddy-induced accelerations are much larger than the accelerations due to planetary-scale waves (cf. to Figs. 10a–d). Moreover, as found for the mean flow composites (Figs. 9f–h), we see that the

synoptic eddy growth and induced accelerations in the North Atlantic basin are strongest in the NOQBO and weakest in the FSST experiment. In particular, the anomalous acceleration pattern induced by synoptic-scale eddy anomalies (Figs. 11b–d) enhances the mean flow anomaly pattern (Figs. 9f–h), with this enhancement being stronger for the NOQBO experiment and weakest for the FSST experiment. This strengthened tropospheric mean flow anomaly is accompanied by strengthening and poleward shift of the tropospheric synoptic wave source (Figs. 11f–h) and Eady growth rate (Figs. 11j–l) anomalies. At the same time, these mean flow baroclinicity anomalies are reinforcing the storm-track anomalies (Figs. 11n–p). This overall suggests that the eddy–mean flow feedback is strongest in the NOQBO experiment and weakest in the FSST experiment, being consistent with their respective tropospheric responses (Fig. 9).

Another obvious explanation for the weaker response in the FSST experiment is the lack of atmosphere–ocean feedbacks in this experiment. This may be because of the adjustment of SSTs to the atmospheric temperatures above reducing the thermal damping on atmospheric anomalies (Barsugli and Battisti 1998). In addition, previous studies have also shown that the wintertime SST tripole in the Atlantic basin can feed back positively to the large-scale atmospheric circulation changes associated with the NAO (Kushnir et al. 2002; Czaja and Frankignoul 2002; Peng et al. 2003; Deser et al. 2007) as well as with other external forcings (Chen et al. 2013; Chen and Schneider 2014). Other studies have also shown that enhanced extratropical SST gradients can lead to a substantial strengthening in eddy activity, storm tracks, and the annular mode in winter (Nakamura et al. 2008; Sampe et al. 2013).

To further examine the possible role of the ocean, we composite the global SST anomalies (Figs. 12a,c,e) and the Atlantic basin meridional SST gradient anomalies (Figs. 12b,d,f). We see a typical positive NAO-related SST-tripole anomaly pattern, with enhanced negative SST gradients in midlatitudes all across the Atlantic ocean, with a slight northeast tilt. Moreover, the southern more positive–negative dipole of the SST gradient pattern coincides with a similar dipole in the anomalous Eady growth rate field (as in Figs. 11i–k plotted on Figs. 12d,f as contour lines). This may suggest that the positive NAO SST-tripole pattern could enhance the anomalies in lower level baroclinicity that further generate synoptic wave activity (Figs. 11b–d) and strengthen the eddy–mean flow feedback during DWC event. We note these SST-tripole-like anomalies, which are shown for the 5 days centered around the DWC events, are already established in the month leading to the DWC peak (see Fig. S6). This apparent ocean preconditioning may be playing an enhancing role, similar to

⁶ The synoptic-scale eddy activity is described by \mathbf{E} vectors [$\mathbf{E} = (\overline{v'^2} - \overline{u'^2}, -\overline{u'v'})$; Hoskins et al. 1983] of the 250-hPa 2–6-day bandpass-filtered winds u' and v' . The overbar signifies a time average and the prime a deviation from this average.

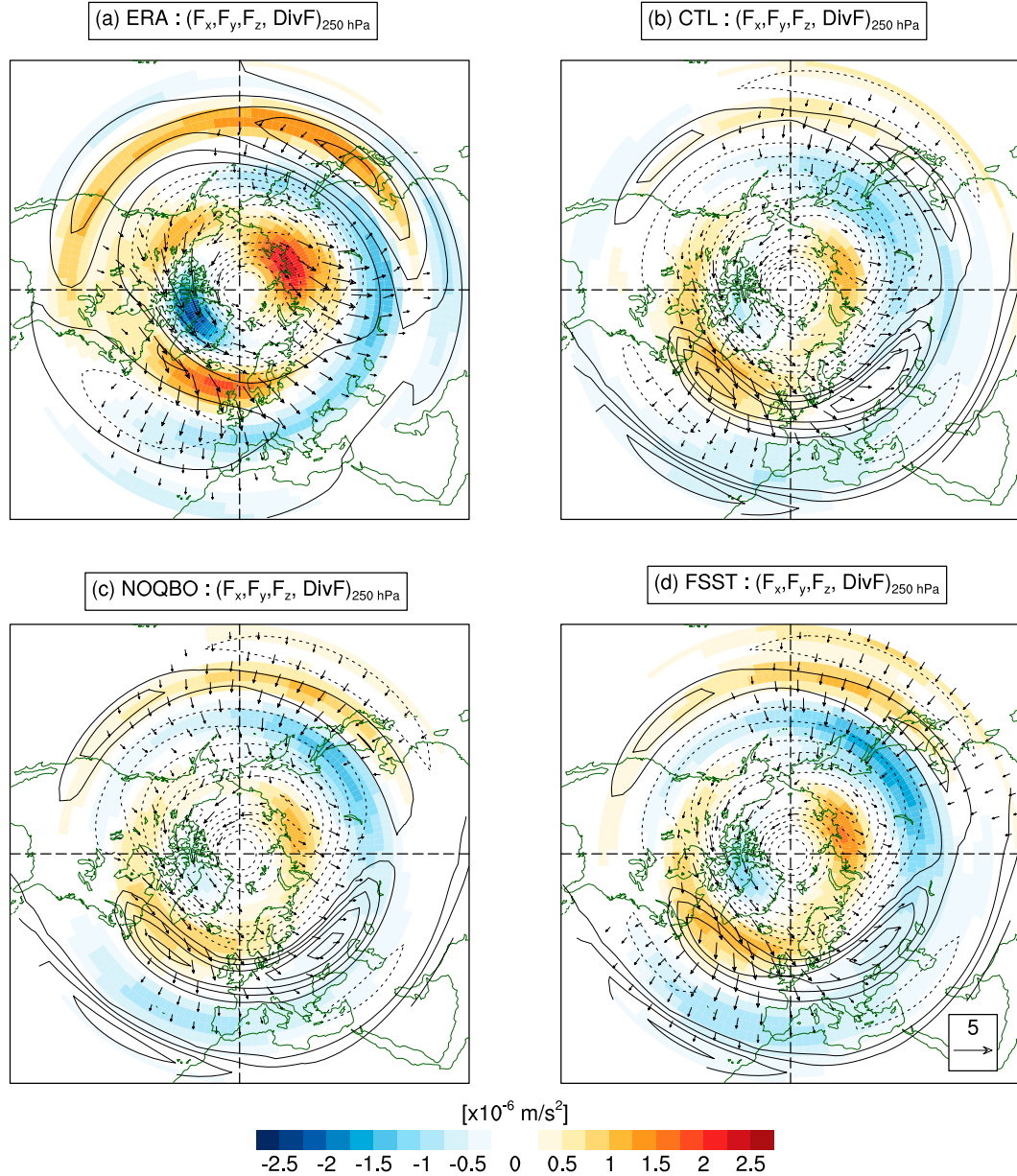


FIG. 10. The composites of planetary-scale wave divergence anomalies (colored shading, $\times 10^{-6} \text{ m s}^{-2}$) at 250 hPa during the period of maximum DWC impact on the troposphere (5-day average around the central date) in JFM for (a) ERA, (b) CTL, (c) NOQBO, and (d) FSST. The \mathbf{F}_s vectors (horizontal components: F_x and F_y) are shown as arrows (m s^{-1}); the vertical vector component (F_z) is given by contours [solid (dashed) upward (downward) planetary-scale wave source]. The shadings are drawn only for anomalies that are statistically significant at the 95% confidence level using a Monte Carlo approach. The \mathbf{F}_s vector is approximately parallel to the wave-energy propagation direction, and its zonal mean is equivalent to the Eliassen–Palm flux. (See the [appendix](#) for a detailed formulation.)

that of SST fronts in a number of idealized model studies (e.g., Nakamura et al. 2008; Brayshaw et al. 2008). However, more detailed studies are needed to understand this effect. The lack of this positive NAO SST-tripole pattern and the weaker synoptic-scale eddy feedback in the fixed SST experiment thus altogether may explain a weaker tropospheric response to DWC in this experiment.

Examining the SST fields in the NOQBO experiment suggests they may also explain part of the differences in this run as well, since the SST anomalies are stronger in this run than in the CTL experiment. Another striking difference between the NOQBO and CTL experiments is the much stronger tropical Pacific cold anomaly in the former (green boxes in the Pacific in Figs. 12c,e). Several

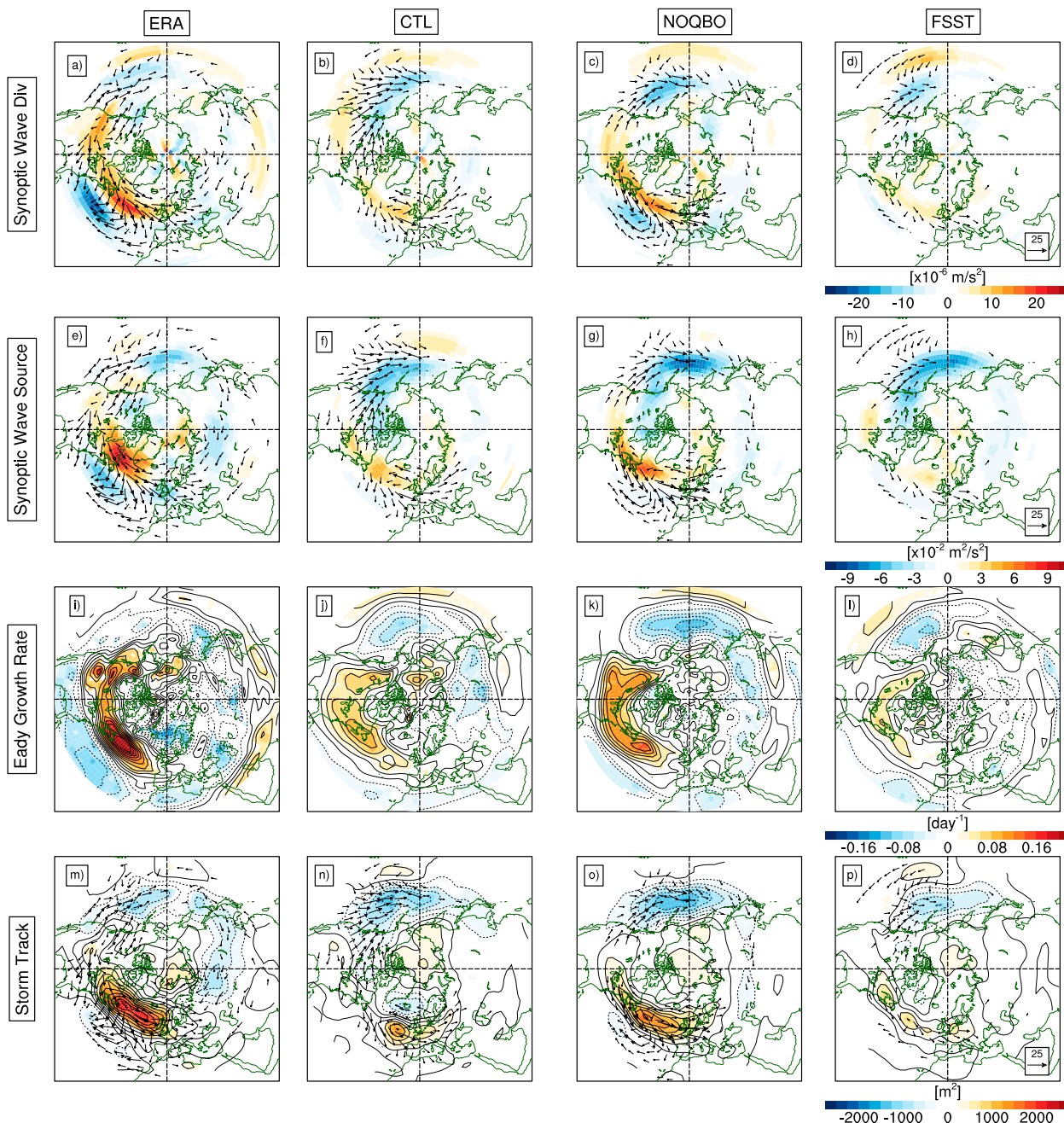


FIG. 11. The composites of (a)–(d) 250-hPa synoptic wave divergence (colored shading, $\times 10^{-6} \text{ m s}^{-2}$), (e)–(h) 700-hPa synoptic wave source (colored shading, $\times 10^{-2} \text{ m}^2 \text{ s}^{-2}$), (i)–(l) 700-hPa Eady's maximum growth rate (colored shading, day^{-1}), and (m)–(p) 250-hPa storm-track anomalies (colored shading, m^2) during the period of maximum DWC impact on the troposphere in JFM. The vectors in (a)–(h) and (m)–(p) are the \mathbf{E} vectors (m s^{-1} with horizontal components E_x and E_y). The vertical component of the \mathbf{E} vectors in (e)–(h) is calculated by $-f\bar{v}'\bar{\theta}'(\partial\theta/\partial p)^{-1}$, representing the synoptic wave source where the positive (negative) values indicate upward (downward) synoptic wave fluxes. The Eady growth rate anomaly in (i)–(l) is calculated by $0.31|f||\partial u/\partial z|/N$. The color shading in (m)–(p) indicates the high-pass (<6-day period) filtered height covariance (Z'^2). The shadings are only drawn for anomalies that are statistically significant at the 95% confidence level using a Monte Carlo approach.

studies have shown that cold (warm) ENSO drives a strengthening (weakening) of the polar vortex, leading to surface anomalies projecting on a positive (negative) NAO-like pattern (Manzini et al. 2006; Ineson and

Scaife 2009). This suggests that the differences in the tropical Pacific SSTs among the model experiments may also contribute to the differences in the strength of the NAO-like response. Nevertheless, it should be noted that

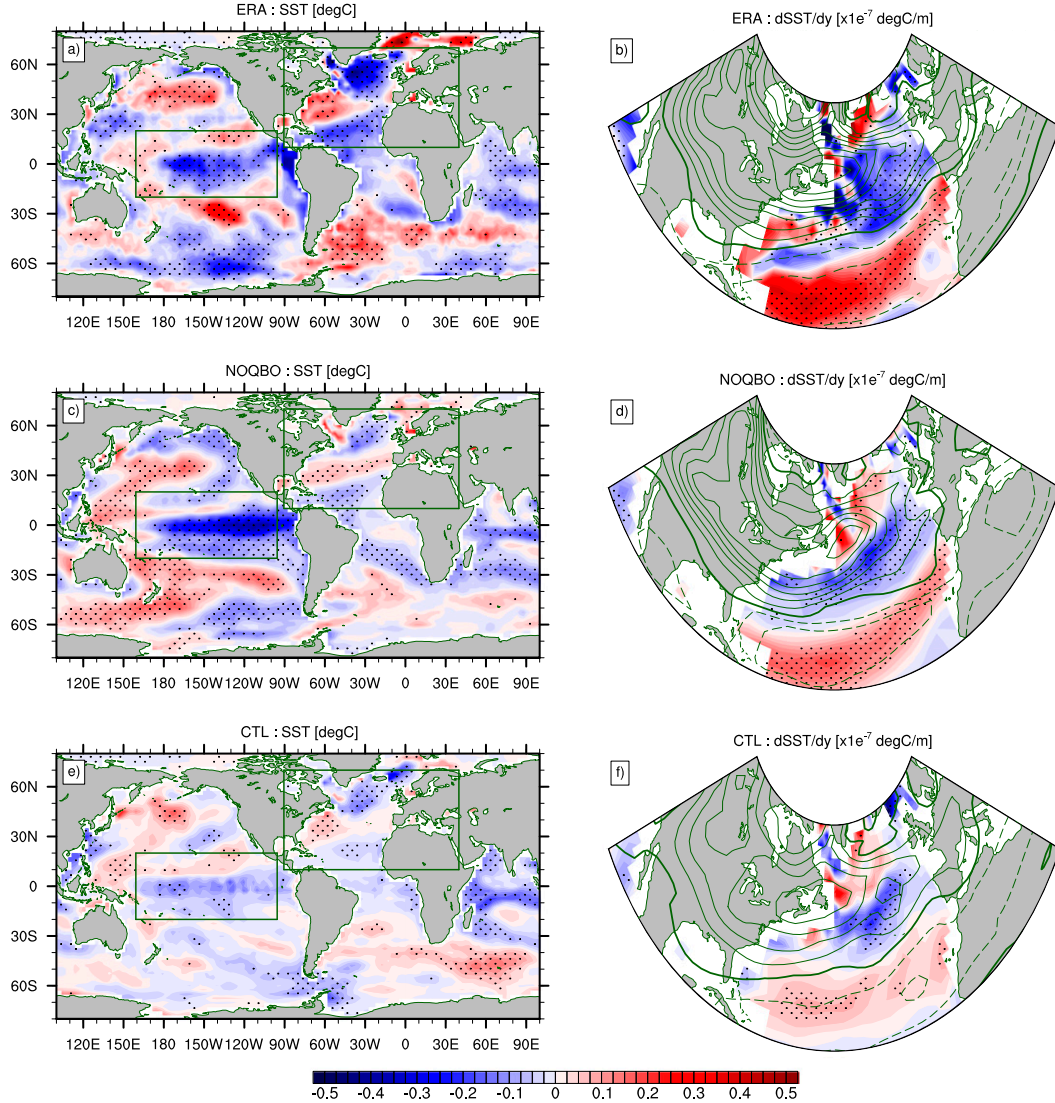


FIG. 12. The composites of (a),(c),(e) global SST anomalies ($^{\circ}\text{C}$) and (b),(d),(f) meridional SST gradient anomalies ($^{\circ}\text{C m}^{-1}$) during the period of maximum DWC impact on the troposphere (i.e., 5-day average around the central date) in JFM for (top to bottom) ERA, NOQBO, and CTL. Green contours indicate the Eady growth rate anomalies (day^{-1}) at 700 hPa. The dots indicate where the anomalies are significant at the 95% confidence level using a Monte Carlo approach.

the remote effect of tropical SST forcing on the NAO typically invokes downward propagation of zonal-mean stratospheric wind anomalies; thus, the connection between downward zonal-mean coupling induced by tropical Pacific SST forcing and the tropospheric impact of DWC needs to be further investigated. Furthermore, the cause for strong differences between the tropical Pacific SSTs in the CTL and NOQBO experiments might at least partly be due to a damping effect of the nudging of lower stratospheric winds on the tropical tropospheric circulation in the CTL experiment, but more detailed studies are needed to understand this effect.

To summarize, the composite analysis indicates that differences in the strength of the following synoptic-scale eddy-mean flow feedbacks can explain the differences in tropospheric response to DWC in the North Atlantic region between the NOQBO and FSST experiments: a strengthening and poleward shift of the tropospheric jet (Figs. 9e–h) is enhanced by the divergence of the anomalous synoptic-scale waves (Figs. 11b–d). This zonal-mean wind strengthening and shifting is accompanied by a strengthening and shifting of the Eady growth rate (Figs. 11j–l) and the synoptic wave sources (Figs. 11f–h), which in turn are consistent with the strengthening and

poleward shifting of the synoptic-scale wave activity (Figs. 11b–d). In addition, the positive–negative dipole of the anomalous Eady growth rate field is consistent with a similar dipole of the anomalous meridional SST gradient in the North Atlantic during a DWC event. These results suggest that the synoptic-scale eddy–mean flow feedbacks and the possible contribution of the SST anomalies during a DWC event play a central role in setting the strength of the tropospheric responses to DWC. The latter might be due to strengthened storm tracks due to stronger SST gradients, reduced thermal damping at the ocean surface, and positive atmosphere–ocean feedbacks, but more detailed studies are needed to examine this and, in particular, to distinguish the effects of interannual SST variability, which is also missing from the fixed SST experiment.

6. Conclusions

In this study, the influence of the QBO and SST variability on downward wave coupling (DWC) and its subsequent impacts on the troposphere–surface system were investigated in CESM1(WACCM) experiments in comparison to ERA data. We performed a set of sensitivity simulations with NCAR’s fully coupled CESM1 (WACCM) model, by systematically switching on and off the QBO and interactive SSTs and sea ice in the model. We address the attribution of these forcing factors on DWC by examining the differences in background wind, wave source, wave–mean flow interaction, and the time-lagged vertical wave-1 coupling as well as the evolution of wave geometry. Afterward, the tropospheric impact of DWC is investigated based on the stratospheric heat flux extremes as proposed by [Shaw et al. \(2014\)](#). Our results can be summarized as follows:

- 1) The CESM1(WACCM) is able to capture the main features of DWC during NH winter (1958–2005). Consistent with the ERA dataset, DWC in the model maximizes during midwinter when the stratospheric basic state exhibits a bounded wave geometry associated with a high-latitude meridional waveguide in the lower stratosphere and a vertical reflecting surface in the upper stratosphere. The model, however, exhibits a bias in its seasonal cycle of DWC (Figs. 3a,b), which is associated with common model biases of the background zonal-mean winds that feed back on the wave dynamics. The results highlight that an accurate representation of the stratospheric basic-state wave geometry is necessary for a proper representation of the seasonal evolution of DWC in CESM1(WACCM).
- 2) Without the QBO nudging, the occurrence of DWC between the stratosphere and the troposphere is

significantly suppressed. This is associated with a less persistent configuration of bounded wave geometries, which allows more wave dispersion in the meridional direction (Figs. 7c,d) and a stronger wave absorption (convergent EP flux) on the equatorward flank of the polar vortex (Figs. S1a–d). In particular, when the QBO nudging is switched off and equatorial winds are permanent easterly, planetary wave propagation from the troposphere into the stratosphere is enhanced, leading to a stronger wave absorption in the upper stratosphere, and thus a weaker DWC activity toward the troposphere (Fig. 5 and Figs. S1a–d). The enhanced wave convergence results in a weakening of the polar night jet (Fig. 5) and a strengthening of the stratospheric residual mean circulation at high latitudes (Figs. S2a–d).

- 3) Without SST variability, in contrast, the occurrence of DWC between the stratosphere and the troposphere is significantly enhanced. The DWC starts earlier and ends later in the seasonal cycle (November–April). This is associated with a longer and more persistent configuration of bounded wave geometries (Figs. 7e,f), which focuses planetary wave reflection in the vertical direction toward the troposphere. An increased DWC activity is consistent with anomalous downward wave flux activity, which leads to stronger wave divergence and thus to stronger DWC activity (Figs. S1e–h). A stronger DWC activity throughout the season is consistent through wave–mean flow interaction with an acceleration of the polar night jet (Figs. 5e–h and Figs. S1e–h) and anomalous weakening of the residual mean circulation (Figs. S2e–h).
- 4) Even though the downward wave-1 coupling is much larger in the FSST experiment and much smaller in the NOQBO experiment, compared to the CTL (Figs. 6, 8), the associated tropospheric changes in the North Atlantic region are weaker for the FSST and stronger for the NOQBO relative to the CTL experiment (Fig. 9). This apparently counterintuitive result might be explained by differences in the strength of the synoptic-scale eddy–mean flow feedbacks and the possible contribution of the ocean and associated SST anomalies between the FSST, the NOQBO, and the CTL experiments.

A recent study by [Hansen et al. \(2014\)](#) using the same model experiments showed that the frequency of major SSWs in winter is significantly reduced (increased) when the SST variability (QBO) is removed in the simulations. It was also reported that the tropospheric impact of major SSWs seems to be less significant and confined to a smaller area when the SST variability is excluded,

while removing the QBO seems to shift the period of significant tropospheric influence by about 10 days. The significant increase (decrease) of SSW frequency in the experiment without QBO (SST variability) is consistent with stronger (weaker) wave absorption in the polar vortex region found in our study, which results in significant decreased (increased) DWC activity between the stratosphere and the troposphere. This suggests a clear dynamical link between the wave absorption in the stratosphere and the probability of the occurrence of SSW and DWC events.

Several other recent studies have documented the importance of the QBO and SST variability as well as its coupling to the ocean on the behavior of SSWs in climate models (e.g., Calvo et al. 2009; Richter et al. 2011; Hansen et al. 2014). Our results show that these two factors are also important for DWC in the model and for establishing a correct representation of stratosphere–troposphere coupling. In particular, these two factors can influence the tropospheric response to DWC both through a modification of wave propagation and interaction with the mean flow in the stratosphere, and through a modification of the internal tropospheric feedbacks, which strongly affect the response to a given DWC event. While the current work represents an advance in our understanding of DWC in response to natural forcing factors, clearly more work is needed to understand the role of the ocean and of other important factors, such as the 11-yr solar cycle, volcanic eruptions, and anthropogenic climate change.

Most of the chemistry–climate models (CCMs) used for the scientific assessment of ozone are not coupled to an interactive ocean (WMO 2011). Our study suggests that the SST variability and thus two-way ocean–atmosphere interaction are important in order to represent stratosphere–troposphere coupling and thus correct responses to recent and future ozone changes.

Acknowledgments. We acknowledge support received from the German–Israeli Foundation for Scientific Research and Development under Grant GIF1151-83.8/2011. This work has also been partially performed within the Helmholtz-University Young Investigators Group NATHAN funded by the Helmholtz Association through the President’s Initiative and Networking Fund and the GEOMAR Helmholtz Centre for Ocean Research Kiel. NH is also partly supported by a Rossby Visiting Fellowship from the International Meteorological Institute (IMI), Stockholm, Sweden. The authors also would like to thank Alan Plumb for discussions on the tropospheric impact of DWC. We are also grateful to Christof Petrick, Felicitas Hansen, and Wuke Wang for setting up the fully coupled model experiments used in

this study. The model simulations were performed at the German Climate Computing Centre [Deutsches Klimarechenzentrum (DKRZ)], Hamburg. Finally, we also acknowledge COST ACTION ES1005 TOSCA for financing the participation of SWL at the first training school on “Solar Variability and Climate Response,” Thessaloniki, Greece, 2013.

APPENDIX

Planetary Wave Forcing of the Mean Flow

To quantify the drag exerted by planetary-scale waves on the zonal-mean flow, the EP flux ($\mathbf{F} = \{F_\phi, F_z\}$) and its divergence $(\rho_0 a \cos \phi)^{-1} \nabla \cdot \mathbf{F}$ are computed in a spherical log–pressure coordinate based on Andrews et al. (1987), where the components are given as follows:

$$F_\phi \equiv \rho_0 a \cos \phi \left(\bar{u}_z \frac{\overline{v'\theta'}}{\bar{\theta}_z} - \overline{v'u'} \right) \quad \text{and} \quad (A1)$$

$$F_z \equiv \rho_0 a \cos \phi \left\{ \left[f - (a \cos \phi)^{-1} (\bar{u} \cos \phi)_\phi \right] \frac{\overline{v'\theta'}}{\bar{\theta}_z} - \overline{w'u'} \right\}, \quad (A2)$$

where u , v , and w are, respectively, the zonal, meridional, and vertical components of the velocity, a is Earth’s radius, f is the Coriolis parameter, ϕ is latitude, z is height (in log–pressure coordinates), ρ_0 is air density, which varies with height as $\exp(-z/H)$, H is the density scale height taken as 7000 m, and θ is potential temperature. The subscript means the derivative with respect to the corresponding coordinate. The primes denote deviations from the zonal means, and overbars indicate zonal means.

In addition, the 3D wave activity flux (Plumb 1985) to diagnose the potential regional sources (sinks) and propagation characteristics of planetary-scale wave activity is computed as follows:

$$\mathbf{F}_s \equiv \frac{p \cos \phi}{p_o} \times \left\{ \begin{array}{c} v'^2 - \frac{1}{2\Omega a \sin 2\phi} \frac{\partial(v'\Phi')}{\partial \lambda} \\ -v'u' + \frac{1}{2\Omega a \sin 2\phi} \frac{\partial(u'\Phi')}{\partial \lambda} \\ \frac{2\Omega \sin \phi}{S} \left[v'T' - \frac{1}{2\Omega a \sin 2\phi} \frac{\partial(T'\Phi')}{\partial \lambda} \right] \end{array} \right\}, \quad (A3)$$

where $S = \partial \hat{T} / \partial z + \kappa \hat{T} / H$ is the static stability (the caret indicating the areal average over the region north of

20°N), Φ is the geopotential, $\kappa = R/c_p \approx 0.286$, λ is longitude, and p_o is 1000 hPa.

REFERENCES

- Andrews, D. G., J. R. Holton, and C. B. Leovy, 1987: *Middle Atmosphere Dynamics*. International Geophysics Series, Vol. 40, Academic Press, 489 pp.
- Baldwin, M. P., and T. J. Dunkerton, 2001: Stratospheric harbingers of anomalous weather regimes. *Science*, **294**, 581–584, doi:10.1126/science.1063315.
- Barsugli, J. J., and D. S. Battisti, 1998: The basic effects of atmosphere–ocean thermal coupling on midlatitude variability. *J. Atmos. Sci.*, **55**, 477–493, doi:10.1175/1520-0469(1998)055<0477:TBEAO>2.0.CO;2.
- Brayshaw, D. J., B. Hoskins, and M. Blackburn, 2008: The storm-track response to idealized SST perturbations in an aquaplanet GCM. *J. Atmos. Sci.*, **65**, 2842–2860, doi:10.1175/2008JAS2657.1.
- Bretherton, C. S., C. Smith, and J. M. Wallace, 1992: An intercomparison of methods for finding coupled patterns in climate data. *J. Climate*, **5**, 541–560, doi:10.1175/1520-0442(1992)005<0541:AIOMFF>2.0.CO;2.
- Calvo, N., M. A. Giorgetta, R. Garcia-Herrera, and E. Manzini, 2009: Nonlinearity of the combined warm ENSO and QBO effects on the Northern Hemisphere polar vortex in MAECHAM5 simulations. *J. Geophys. Res.*, **114**, D13109, doi:10.1029/2008JD011445.
- Charney, J. G., and P. G. Drazin, 1961: Propagation of planetary-scale disturbances from the lower into the upper atmosphere. *J. Geophys. Res.*, **66**, 83–109, doi:10.1029/JZ066i001p00083.
- Chen, H., and E. K. Schneider, 2014: Comparison of the SST-forced responses between coupled and uncoupled climate simulations. *J. Climate*, **27**, 740–756, doi:10.1175/JCLI-D-13-00092.1.
- , —, B. P. Kirtman, and I. Colfescu, 2013: Evaluation of weather noise and its role in climate model simulations. *J. Climate*, **26**, 3766–3784, doi:10.1175/JCLI-D-12-00292.1.
- Czaja, A., and C. Frankignoul, 2002: Observed impact of Atlantic SST anomalies on the North Atlantic Oscillation. *J. Climate*, **15**, 606–623, doi:10.1175/1520-0442(2002)015<0606:OIOASA>2.0.CO;2.
- Dee, D. P., and Coauthors, 2011: The ERA-Interim reanalysis: Configuration and performance of the data assimilation system. *Quart. J. Roy. Meteor. Soc.*, **137**, 553–597, doi:10.1002/qj.828.
- Deser, C., R. A. Tomas, and S. Peng, 2007: The transient atmospheric circulation response to North Atlantic SST and sea ice anomalies. *J. Climate*, **20**, 4751–4767, doi:10.1175/JCLI4278.1.
- Dunn-Sigouin, E., and T. A. Shaw, 2015: Comparing and contrasting extreme stratospheric events, including their coupling to the tropospheric circulation. *J. Geophys. Res. Atmos.*, **120**, 1374–1390, doi:10.1002/2014JD022116.
- Eliassen, A., and E. Palm, 1961: *On the Transfer of Energy in Stationary Mountain Waves*. I Kommisjon hos Aschehoug, 23 pp.
- Garfinkel, C. I., T. A. Shaw, D. L. Hartmann, and D. W. Waugh, 2012: Does the Holton–Tan mechanism explain how the quasi-biennial oscillation modulates the Arctic polar vortex? *J. Atmos. Sci.*, **69**, 1713–1733, doi:10.1175/JAS-D-11-0209.1.
- , D. W. Waugh, and E. P. Gerber, 2013: The effect of tropospheric jet latitude on coupling between the stratospheric polar vortex and the troposphere. *J. Climate*, **26**, 2077–2095, doi:10.1175/JCLI-D-12-00301.1.
- Gent, P. R., and Coauthors, 2011: The Community Climate System Model version 4. *J. Climate*, **24**, 4973–4991, doi:10.1175/2011JCLI4083.1.
- Gray, L. J., and Coauthors, 2010: Solar influences on climate. *Rev. Geophys.*, **48**, RG4001, doi:10.1029/2009RG000282.
- Hamilton, K., 1993: An examination of observed Southern Oscillation effects in the Northern Hemisphere stratosphere. *J. Atmos. Sci.*, **50**, 3468–3474, doi:10.1175/1520-0469(1993)050<3468:AEOOSO>2.0.CO;2.
- Hansen, F., K. Matthes, and L. J. Gray, 2013: Sensitivity of stratospheric dynamics and chemistry to QBO nudging width in the chemistry–climate model WACCM. *J. Geophys. Res. Atmos.*, **118**, 10 464–10 474, doi:10.1002/jgrd.50812.
- , —, C. Petrick, and W. Wang, 2014: The influence of natural and anthropogenic factors on major stratospheric sudden warmings. *J. Geophys. Res. Atmos.*, **119**, 8117–8136, doi:10.1002/2013JD021397.
- Harnik, N., 2009: Observed stratospheric downward reflection and its relation to upward pulses of wave activity. *J. Geophys. Res.*, **114**, D08120, doi:10.1029/2008JD010493.
- , and R. S. Lindzen, 2001: The effect of reflecting surfaces on the vertical structure and variability of stratospheric planetary waves. *J. Atmos. Sci.*, **58**, 2872–2894, doi:10.1175/1520-0469(2001)058<2872:TEORSO>2.0.CO;2.
- Holton, J. R., and H.-C. Tan, 1980: The influence of the equatorial quasi-biennial oscillation on the global circulation at 50 mb. *J. Atmos. Sci.*, **37**, 2200–2208, doi:10.1175/1520-0469(1980)037<2200:TIOTEQ>2.0.CO;2.
- Hoskins, B. J., I. N. James, and G. H. White, 1983: The shape, propagation and mean-flow interaction of large-scale weather systems. *J. Atmos. Sci.*, **40**, 1595–1612, doi:10.1175/1520-0469(1983)040<1595:TSPAMF>2.0.CO;2.
- Hurrell, J. W., Y. Kushnir, G. Ottersen, and M. Visbeck, 2013: An overview of the North Atlantic Oscillation. *The North Atlantic Oscillation: Climatic Significance and Environmental Impact*, J. W. Hurrell et al., Eds., Amer. Geophys. Union, 1–35, doi:10.1029/134GM01.
- Hurwitz, M. M., P. A. Newman, and C. I. Garfinkel, 2012: On the influence of North Pacific sea surface temperature on the Arctic winter climate. *J. Geophys. Res.*, **117**, D19110, doi:10.1029/2012JD017819.
- Ineson, S., and A. Scaife, 2009: The role of the stratosphere in the European climate response to El Niño. *Nat. Geosci.*, **2**, 32–36, doi:10.1038/ngeo381.
- Jaiser, R., K. Dethloff, and D. Handorf, 2013: Stratospheric response to Arctic sea ice retreat and associated planetary wave propagation changes. *Tellus*, **65A**, 19375, doi:10.3402/tellusa.v65i0.19375.
- Keenlyside, N., and N.-E. Omrani, 2014: Has a warm North Atlantic contributed to recent European cold winters? *Environ. Res. Lett.*, **9**, 061001, doi:10.1088/1748-9326/9/6/061001.
- Kinnison, D. E., and Coauthors, 2007: Sensitivity of chemical tracers to meteorological parameters in the MOZART-3 chemical transport model. *J. Geophys. Res.*, **112**, D20302, doi:10.1029/2006JD007879.
- Kunz, T., and R. J. Greatbatch, 2013: On the northern annular mode surface signal associated with stratospheric variability. *J. Atmos. Sci.*, **70**, 2103–2118, doi:10.1175/JAS-D-12-0158.1.
- Kushnir, Y., W. Robinson, I. Blad, N. Hall, S. Peng, and R. Sutton, 2002: Atmospheric GCM response to extratropical SST anomalies: Synthesis and evaluation. *J. Climate*, **15**, 2233–2256, doi:10.1175/1520-0442(2002)015<2233:AGRTES>2.0.CO;2.

- Labitzke, K., 1982: On the interannual variability of the middle stratosphere during the northern winters. *J. Meteor. Soc. Japan*, **60**, 124–139.
- Li, Y., and N.-C. Lau, 2013: Influences of ENSO on stratospheric variability, and the descent of stratospheric perturbations into the lower troposphere. *J. Climate*, **26**, 4725–4748, doi:[10.1175/JCLI-D-12-00581.1](https://doi.org/10.1175/JCLI-D-12-00581.1).
- Limpasuvan, V., and D. L. Hartmann, 2000: Wave-maintained annular modes of climate variability. *J. Climate*, **13**, 4414–4429, doi:[10.1175/1520-0442\(2000\)013<4414:WMAMOC>2.0.CO;2](https://doi.org/10.1175/1520-0442(2000)013<4414:WMAMOC>2.0.CO;2).
- Lorenz, D. J., and D. L. Hartmann, 2003: Eddy–zonal flow feedback in the Northern Hemisphere winter. *J. Climate*, **16**, 1212–1227, doi:[10.1175/1520-0442\(2003\)16<1212:EFFITN>2.0.CO;2](https://doi.org/10.1175/1520-0442(2003)16<1212:EFFITN>2.0.CO;2).
- Lu, H., T. J. Bracegirdle, T. Phillips, A. Bushell, and L. Gray, 2014: Mechanisms for the Holton–Tan relationship and its decadal variation. *J. Geophys. Res. Atmos.*, **119**, 2811–2830, doi:[10.1002/2013JD021352](https://doi.org/10.1002/2013JD021352).
- Manzini, E., M. A. Giorgetta, M. Esch, L. Kornblueh, and E. Roeckner, 2006: The influence of sea surface temperatures on the northern winter stratosphere: Ensemble simulations with the MAECHAM5 model. *J. Climate*, **19**, 3863–3881, doi:[10.1175/JCLI3826.1](https://doi.org/10.1175/JCLI3826.1).
- Marsh, D. R., R. R. Garcia, D. E. Kinnison, B. A. Boville, F. Sassi, S. C. Solomon, and K. Matthes, 2007: Modeling the whole atmosphere response to solar cycle changes in radiative and geomagnetic forcing. *J. Geophys. Res.*, **112**, D23306, doi:[10.1029/2006JD008306](https://doi.org/10.1029/2006JD008306).
- , M. J. Mills, D. E. Kinnison, J.-F. Lamarque, N. Calvo, and L. M. Polvani, 2013: Climate change from 1850 to 2005 simulated in CESM1(WACCM). *J. Climate*, **26**, 7372–7391, doi:[10.1175/JCLI-D-12-00558.1](https://doi.org/10.1175/JCLI-D-12-00558.1).
- Matsuno, T., 1970: Vertical propagation of stationary planetary waves in the winter Northern Hemisphere. *J. Atmos. Sci.*, **27**, 871–883, doi:[10.1175/1520-0469\(1970\)027<0871:VPOSPW>2.0.CO;2](https://doi.org/10.1175/1520-0469(1970)027<0871:VPOSPW>2.0.CO;2).
- Matthes, K., D. R. Marsh, R. R. Garcia, D. E. Kinnison, F. Sassi, and S. Walters, 2010: Role of the QBO in modulating the influence of the 11 year solar cycle on the atmosphere using constant forcings. *J. Geophys. Res.*, **115**, D18110, doi:[10.1029/2009JD013020](https://doi.org/10.1029/2009JD013020).
- McIntyre, M. E., and T. N. Palmer, 1983: Breaking planetary waves in the stratosphere. *Nature*, **305**, 593–600, doi:[10.1038/305593a0](https://doi.org/10.1038/305593a0).
- Nakamura, H., T. Sampe, A. Goto, W. Ohfuchi, and S.-P. Xie, 2008: On the importance of midlatitude oceanic frontal zones for the mean state and dominant variability in the tropospheric circulation. *Geophys. Res. Lett.*, **35**, L15709, doi:[10.1029/2008GL034010](https://doi.org/10.1029/2008GL034010).
- Omrani, N.-E., N. Keenlyside, J. Bader, and E. Manzini, 2014: Stratosphere key for wintertime atmospheric response to warm Atlantic decadal conditions. *Climate Dyn.*, **42**, 649–663, doi:[10.1007/s00382-013-1860-3](https://doi.org/10.1007/s00382-013-1860-3).
- , J. Bader, N. Keenlyside, and E. Manzini, 2016: Troposphere–stratosphere response to large-scale North Atlantic Ocean variability in an atmosphere/ocean coupled model. *Climate Dyn.*, **46**, 1397–1415, doi:[10.1007/s00382-015-2654-6](https://doi.org/10.1007/s00382-015-2654-6), in press.
- Peng, S., W. A. Robinson, and S. Li, 2003: Mechanisms for the NAO responses to the North Atlantic SST tripole. *J. Climate*, **16**, 1987–2004, doi:[10.1175/1520-0442\(2003\)016<1987:MFTNRT>2.0.CO;2](https://doi.org/10.1175/1520-0442(2003)016<1987:MFTNRT>2.0.CO;2).
- Perlwitz, J., and N. Harnik, 2003: Observational evidence of a stratospheric influence on the troposphere by planetary wave reflection. *J. Climate*, **16**, 3011–3026, doi:[10.1175/1520-0442\(2003\)016<3011:OEOASI>2.0.CO;2](https://doi.org/10.1175/1520-0442(2003)016<3011:OEOASI>2.0.CO;2).
- Plumb, R., 1985: On the three-dimensional propagation of stationary waves. *J. Atmos. Sci.*, **42**, 217–229, doi:[10.1175/1520-0469\(1985\)042<0217:OTTDPO>2.0.CO;2](https://doi.org/10.1175/1520-0469(1985)042<0217:OTTDPO>2.0.CO;2).
- Richter, J. H., K. Matthes, N. Calvo, and L. J. Gray, 2011: Influence of the quasi-biennial oscillation and El Niño–Southern Oscillation on the frequency of sudden stratospheric warmings. *J. Geophys. Res.*, **116**, D20111, doi:[10.1029/2011JD015757](https://doi.org/10.1029/2011JD015757).
- Robock, A., 2000: Volcanic eruptions and climate. *Rev. Geophys.*, **38**, 191–219, doi:[10.1029/1998RG000054](https://doi.org/10.1029/1998RG000054).
- Sampe, T., H. Nakamura, and A. Goto, 2013: Potential influence of a midlatitude oceanic frontal zone on the annular variability in the extratropical atmosphere as revealed by aqua-planet experiments. *J. Meteor. Soc. Japan*, **91A**, 243–267, doi:[10.2151/jmsj.2013-A09](https://doi.org/10.2151/jmsj.2013-A09).
- Schimanke, S., T. Spanghel, H. Huebener, and U. Cubasch, 2013: Variability and trends of major stratospheric warmings in simulations under constant and increasing GHG concentrations. *Climate Dyn.*, **40**, 1733–1747, doi:[10.1007/s00382-012-1530-x](https://doi.org/10.1007/s00382-012-1530-x).
- Schreck, C. J., L. Shi, J. P. Kossin, and J. J. Bates, 2013: Identifying the MJO, equatorial waves, and their impacts using 32 years of HIRS upper-tropospheric water vapor. *J. Climate*, **26**, 1418–1431, doi:[10.1175/JCLI-D-12-00034.1](https://doi.org/10.1175/JCLI-D-12-00034.1).
- Shaw, T. A., and J. Perlwitz, 2013: The life cycle of Northern Hemisphere downward wave coupling between the stratosphere and troposphere. *J. Climate*, **26**, 1745–1763, doi:[10.1175/JCLI-D-12-00251.1](https://doi.org/10.1175/JCLI-D-12-00251.1).
- , —, and N. Harnik, 2010: Downward wave coupling between the stratosphere and troposphere: The importance of meridional wave guiding and comparison with zonal-mean coupling. *J. Climate*, **23**, 6365–6381, doi:[10.1175/2010JCLI3804.1](https://doi.org/10.1175/2010JCLI3804.1).
- , —, and O. Weiner, 2014: Troposphere–stratosphere coupling: Links to North Atlantic weather and climate, including their representation in CMIP5 models. *J. Geophys. Res. Atmos.*, **119**, 5864–5880, doi:[10.1002/2013JD021191](https://doi.org/10.1002/2013JD021191).
- Song, Y., and W. A. Robinson, 2004: Dynamical mechanisms for stratospheric influences on the troposphere. *J. Atmos. Sci.*, **61**, 1711–1725, doi:[10.1175/1520-0469\(2004\)061<1711:DMFSIO>2.0.CO;2](https://doi.org/10.1175/1520-0469(2004)061<1711:DMFSIO>2.0.CO;2).
- SPARC CCMVal, 2010: SPARC report on the evaluation of chemistry-climate models. Stratosphere–Troposphere Processes and Their Role in Climate Tech. Rep. 5, WCRP-132, WMO/TD-1526, 426 pp. [Available online at <http://www.sparc-climate.org/publications/sparc-reports/sparc-report-no5/>.]
- Uppala, S. M., and Coauthors, 2005: The ERA-40 Re-Analysis. *Quart. J. Roy. Meteor. Soc.*, **131**, 2961–3012, doi:[10.1256/qj.04.176](https://doi.org/10.1256/qj.04.176).
- van Loon, H., and K. Labitzke, 1987: The Southern Oscillation. Part V: The anomalies in the lower stratosphere of the Northern Hemisphere in winter and a comparison with the quasi-biennial oscillation. *Mon. Wea. Rev.*, **115**, 357–369, doi:[10.1175/1520-0493\(1987\)115<0357:TSOPVT>2.0.CO;2](https://doi.org/10.1175/1520-0493(1987)115<0357:TSOPVT>2.0.CO;2).
- WMO, 2011: Scientific assessment of ozone depletion: 2010. Global Ozone Research and Monitoring Project Rep. 52, 516 pp.